Published OnlineFirst April 14, 2009; DOI: 10.1158/0008-5472.CAN-08-4242

Research Article

Computationally Guided Photothermal Tumor Therapy Using Long-Circulating Gold Nanorod Antennas

Geoffrey von Maltzahn,[1] Ji-Ho Park,[2] Amit Agrawal,[1] Nanda Kishor Bandaru,[3] Sarit K. Das,[3] Michael J. Sailor,[2] and Sangeeta N. Bhatia[1,4]

[1]Harvard-Massachusetts Institute of Technology Division of Health Sciences and Technology, Cambridge, Massachusetts; [2]Materials Science and Engineering Program, Department of Chemistry and Biochemistry, University of California, San Diego, La Jolla, California; [3]Department of Mechanical Engineering, Indian Institute of Technology Madras, Chennai, India; and [4]Howard Hughes Medical Institute and Electrical Engineering and Computer Science, Massachusetts Institute of Technology/Brigham and Women's Hospital, Boston, Massachusetts

Abstract

Plasmonic nanomaterials have the opportunity to considerably improve the specificity of cancer ablation by i.v. homing to tumors and acting as antennas for accepting externally applied energy. Here, we describe an integrated approach to improved plasmonic therapy composed of multimodal nanomaterial optimization and computational irradiation protocol development. We synthesized polyethylene glycol (PEG)–protected gold nanorods (NR) that exhibit superior spectral bandwidth, photothermal heat generation per gram of gold, and circulation half-life *in vivo* ($t_{1/2}$, ~17 hours) compared with the prototypical tunable plasmonic particles, gold nanoshells, as well as ~2-fold higher X-ray absorption than a clinical iodine contrast agent. After intratumoral or i.v. administration, we fuse PEG-NR biodistribution data derived via noninvasive X-ray computed tomography or *ex vivo* spectrometry, respectively, with four-dimensional computational heat transport modeling to predict photothermal heating during irradiation. In computationally driven pilot therapeutic studies, we show that a single i.v. injection of PEG-NRs enabled destruction of all irradiated human xenograft tumors in mice. These studies highlight the potential of integrating computational therapy design with nanotherapeutic development for ultraselective tumor ablation. [Cancer Res 2009;69(9):3892–900]

Introduction

The electromagnetic properties of plasmonic nanomaterials have been harnessed to develop ultrasensitive diagnostic (1, 2), spectroscopic (3, 4), and, recently, therapeutic technologies (5–8). In particular, tunable plasmonic nanomaterials have attracted attention for their immense optical absorption coefficients and potential as injectable nanoantennas that target tumors and locally convert otherwise benign electromagnetic energy to thermal energy for ablation. Currently, tumor ablation approaches in clinical practice, including radio frequency, laser, and focused ultrasound methods, lack intrinsic tumor specificity to energy absorption. The inability to selectively heat tumor tissues over surrounding compartments necessitates efforts to externally direct applied energy toward tumor tissues, making effective treatment of tumor margins and complex tumor geometries very challenging. By providing a tumor-specific heat source, nanoantennas could considerably broaden the clinical applicability of thermal therapies by simplifying their integration with current therapeutic practices (including improving margin clearance in surgery and synergizing with regional radiation therapies) and reducing morbidity due to off-target heating. Furthermore, by pulsing the external energy source used, tumor-targeted nanoantennas can theoretically ablate with single-cell precision, thereby providing improved accuracy over standard surgical methods and opening the possibility of precisely treating complex tumor margins in sensitive tissues.

To date, preparations of gold nanoshells and nanorods (NR) have shown considerable efficacy for tumor ablation using NIR light (5, 6, 9, 10), with the most recent data showing complete resorption of ~55% and ~25% of irradiated tumors, respectively (11, 12). These results highlight the clinical promise of these technologies and also motivate the further development of superior nanomaterials and improved methods for optimizing irradiation regimens, which could synergistically improve photothermal therapies. From a material perspective, the development of nanoantennas with enhanced circulation times *in vivo,* increased absorption coefficients per weight, and narrower absorption spectra would more efficiently permeate into tumors after i.v. administration, amplify the photothermal contrast between antennas and normal tissue, and allow improved tumor treatment at lower laser intensities or at greater depths *in vivo*. From a procedural perspective, despite a rich history of heat transfer modeling in the hyperthermia field, the use of quantitative modeling to predict the *in vivo* function of plasmonic nanomaterials has widely remained absent from their testing (5, 6, 9, 11, 12). Because the efficacy of photothermal therapy is driven by both the potency of nanoantenna absorption in tumors and the dose of near-IR irradiation, translation of plasmonic materials to effective clinical use will benefit from cohesive integration of biodistribution data with photothermal modeling to predict and customize the four-dimensional irradiated temperature profiles in tumors.

Recently, rod-shaped gold nanoparticles have emerged as precisely tunable plasmonic nanomaterials that may be synthesized in bulk, have narrow size distributions, optical absorption coefficients 10^4-fold to 10^6-fold higher than conventional organic fluorochromes, and theoretical per micron absorption coefficients exceeding those of NIR-absorbing gold nanoshells (13–15). The long precedence of gold nanoparticles in clinical rheumatoid arthritis therapies make gold NRs appealing new candidates for nanoantenna-based photothermal ablation and a wide array of other biomedical applications. Already, gold NRs have been used for a diversity of biological purposes, including multiplexed *in vitro* detection (16), two-photon fluorescence imaging (17), and

Note: Supplementary data for this article are available at Cancer Research Online (http://cancerres.aacrjournals.org/).

Requests for reprints: Sangeeta N. Bhatia, Massachusetts Institute of Technology, 77 Massachusetts Avenue, E19-502D, Cambridge, MA 02139. Phone: 617-324-0221; Fax: 617-324-0740; E-mail: sbhatia@mit.edu.

doi:10.1158/0008-5472.CAN-08-4242

Published OnlineFirst April 14, 2009; DOI: 10.1158/0008-5472.CAN-08-4242

photothermal heating of tumor and bacterial cell targets (7, 8, 12, 18–20). In addition to their plasmon resonance, the larger atomic number and high material density of gold nanomaterials ($z = 79$, $\rho = 19.3$ g/cm^3) compared with clinical formulations of iodine-based reagents ($z = 53$) have attracted interest for X-ray computed tomography (CT) angiography and a few spherical nanoparticle reagents have been developed for *in vivo* use (21, 22).

In this report, we describe the development of polyethylene glycol (PEG)–coated gold NRs as highly absorbing nanoantennas for photothermal tumor destruction under the guidance of biodistribution-based photothermal modeling. We chose a PEG polymer coating due to the widespread clinical use of variable-length PEG polymers for extending the circulation time of protein therapeutics (23, 24) and for nanoparticle formulations, such as the drug-loaded liposomes Doxil. We find that PEG-NRs are highly stable, relatively noncytotoxic *in vitro*, superior photothermal antennas compared with a gold nanoshell preparation *in vitro* and are improved X-ray absorbing agents compared with clinical iodine standard. After i.v. administration, we find PEG-NRs to be among the longest circulating inorganic nanomaterials described to date ($t_{1/2}$, ~17 hours) allowing passive accumulation into xenograft tumors. Using four-dimensional biodistribution-based heat transfer simulations, we designed a therapeutic irradiation regimen that was able to fully destroy all irradiated tumors on mice injected with PEG-NRs using half the light intensity of previous nanoshell therapies.

Materials and Methods

Preparation of PEG-coated gold NRs. Highly stable, ~13 × 47 nm (Fig. 1*A*) cetyltrimethylammonium bromide (CTAB)–coated gold NRs with longitudinal plasmon resonance at 810 nm (Nanopartz, a division of Concurrent Analytical, Inc.) were centrifuged at 16,000 rcf to concentrate and gently resuspended in 250 μmol/L 5-kDa methyl-PEG-thiol (Laysan Bio, Inc.). Thiol activity of polymers was quantified spectraphotometrically using 5,5-dithiobis(2-nitrobenzoic acid) (Sigma) against a DTT (Sigma) gradient to verify that polymer stocks were fully reduced. The solution of 5-kDa methyl-PEG-thiol and CTAB-coated gold NRs was gently mixed at room temperature for 1 h and dialyzed exhaustively against ultrapure water (18 MΩ cm^{-1}) via cellulose ester membrane dialysis to drive PEG addition (Spectrapor). Dialyzed samples were filtered through 100-kDa filters (Millipore) to remove excess polymer and stored at 4°C. To quantify the number of polymers per particle, NRs were coated as described with an amino-PEG-thiol polymer. After dialysis and extensive filtration on 100-kDa centrifugal filters, amino NRs were harvested and an SPDP assay was performed to quantify the number of amines (25).

Stability and cytotoxicity. Solutions of PEG-NRs or CTAB-NRs (~60 μg Au/mL) were normalized and incubated in PBS or 10% human serum for extended periods of time. At regular intervals, samples were spectrophotometrically analyzed for plasmon resonance peak shifts, which would indicate particle aggregation. To assess material toxicity, micropatterned primary hepatocyte/human fibroblast cocultures were prepared as described previously (26). At 24 h after liver coculture seeding, coculture wells were exposed in triplicate to a gradient of PEG-NRs (0–280 μg Au/mL) and allowed to incubate for 24 h. At this point, PEG-NRs were removed, cells were washed repeatedly, and viability was assessed via a 3-(4,5-dimethylthiazol-2-yl)-2,5-diphenyltetrazolium bromide viability assay (Sigma), a colorimetric viability assay for mitochondrial dehydrogenase enzyme activity read using a spectrophotometer (SpectraMax, Molecular Devices).

Photothermal comparison between PEG-NRs and PEG-nanoshells. Gold nanoshells (Nanocomposix) with 120 nm silica core and ~15 nm gold shell were mixed with methyl-PEG-thiol as described (5, 6, 9). Both PEG-nanoshells and PEG-NRs were brought to 7 μg Au/mL, as determined by inductively coupled plasma mass spectrometry (ICP-MS). Tubes containing

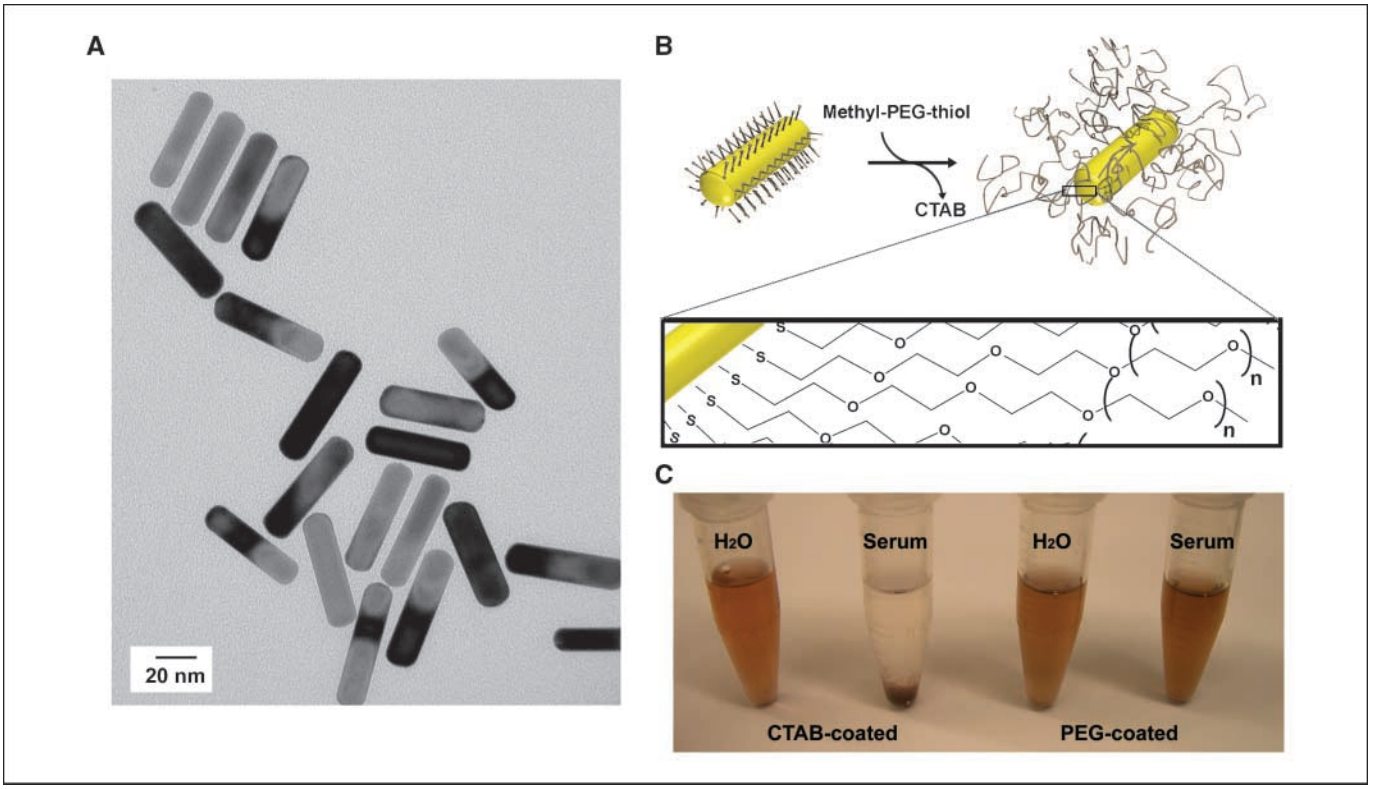

Figure 1. Structure and synthesis of highly absorbing, PEG-protected gold NRs. *A,* near-IR absorbing (810 nm longitudinal plasmon resonance peak) gold NRs were imaged via transmission electron microscopy. *B,* schematic of process to drive CTAB-NR conversion to PEG-NRs under dialysis with rendering and molecular schematic of PEG coating on NR surface. *C,* PEG-NRs show prolonged stability in biological media (>1,000 h), whereas CTAB-coated NRs precipitated over time.

Published OnlineFirst April 14, 2009; DOI: 10.1158/0008-5472.CAN-08-4242

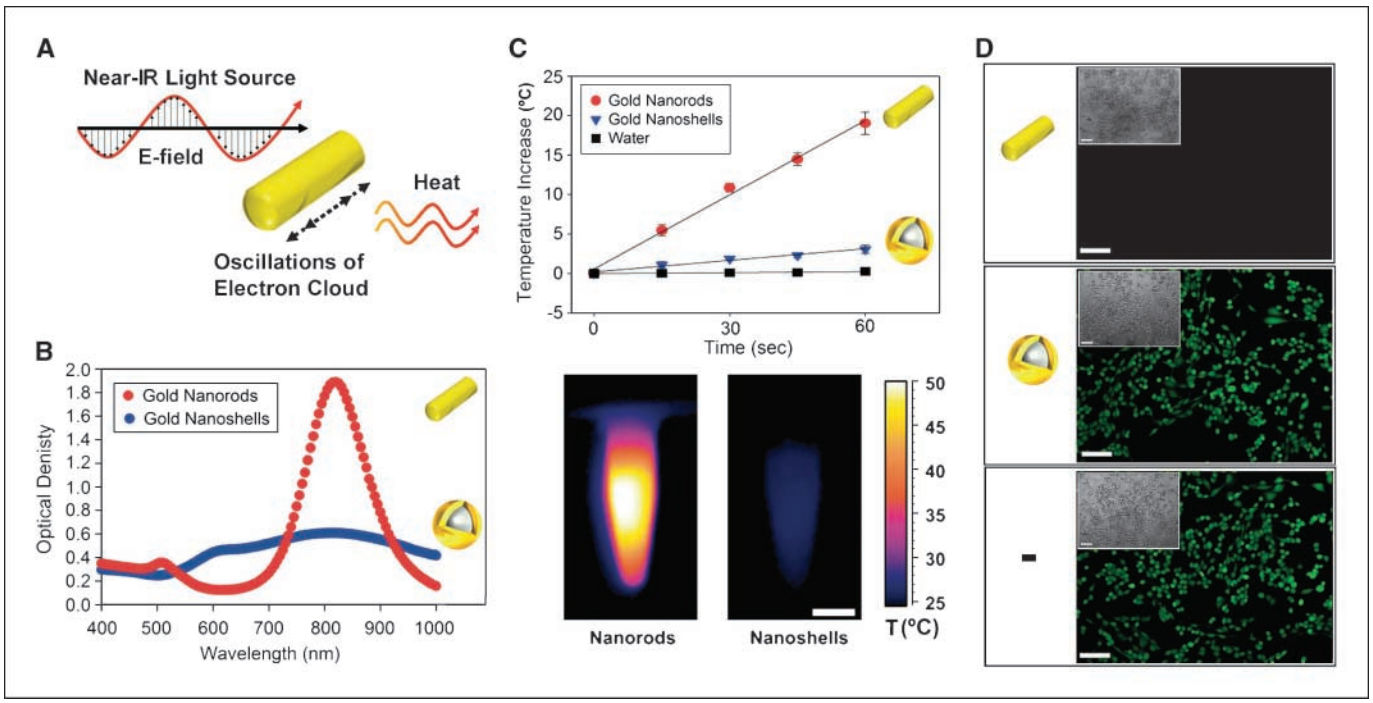

Figure 2. Spectral and photothermal properties of highly absorbing gold NRs compared with gold nanoshells. *A,* schematic of photothermal heating of gold NRs. The dimensions of gold NRs are tuned to have a near-IR plasmon resonance, at which point nanoparticle electrons resonantly oscillate and dissipate energy as heat. *B,* spectra for PEG-gold NRs (*red*) and PEG-gold nanoshells (*blue*), a benchmark for tunable plasmonic nanomaterials, at equal gold concentrations. *C, top,* rate of temperature increase for triplicate PEG-NR and PEG-gold nanoshell solutions (7 μg Au/mL, 810 nm laser, 2 W/cm^2, n = 3 each). *Bottom,* IR thermographic image of PEG-NRs versus PEG-gold nanoshells after 2 min of irradiation. *Scale bar,* 5 mm. *D, in vitro* photothermal toxicity of PEG-NRs over human cancer cells in culture (MDA-MB-435). Tumor cells were incubated with PEG-NRs (14 μg/mL; *top*), PEG-nanoshells (14 μg/mL; *middle*), or media alone (*bottom*) and treated with laser irradiation (2 W/cm^2, 810 nm, 5 min). Calcein AM staining indicates destruction of cells with PEG-NRs, whereas cells irradiated in the presence of nanoshells or media remained viable. Phase region of calcein staining inset. *Scale bar,* 10 μm.

200 μL of these solutions were broadly irradiated, under identical conditions, by an 810-nm diode laser (RPMC Lasers, Inc.) at 2 W/cm^2. During irradiation, an IR thermographic camera (FLIR, Thermacam S60) was used to measure peak sample surface temperature. To assess photothermal cell toxicity, MDA-MB-435 human cancer cells [American Type Culture Collection (ATCC)] were cultured in a 96-well microplate and grown to 80% confluency using ATCC-recommended media. Cells were incubated with either PEG-NRs (14 μg/mL), PEG-nanoshells (14 μg/mL), or media alone. For each, triplicate wells were exposed to the diode laser light (5 min, 2 W/cm^2) or no laser. After treatment, cells were incubated with Calcein AM (5 μg/mL in culture medium; 1 h incubation, Invitrogen), a fluorescent indicator of esterase activity in viable cells and imaged using phase and fluorescence microscopy.

X-ray CT of PEG-NRs. PEG-NRs were suspended in PBS after concentration via membrane centrifugation and serially diluted over a 1,000-fold concentration gradient. A clinical iodine standard was similarly diluted for comparison (Isovue-370). X-ray CT was performed in a GE eXplore Locus microCT scanner (80 kV, 450 μA, 45-μm resolution). For *in vivo* imaging, mice were imaged before NR injection to reveal the baseline level of soft tissue X-ray contrast. Ten microliters of PEG-NRs (~3 pmol) were injected with a 30-gauge needle directly into the center of the tumor, and the needle was maintained in place for ~10 s to allow the tumor to accommodate the additional fluid. After intratumoral administration, mice were imaged and irradiated (~0.75 W/cm^2, 810 nm). X-ray CT images were exported as DICOM files for exportation into modeling software (see Supporting Materials and Methods).

ICP-MS. Samples for ICP-MS (Thermo-Scientific Finnigan ELEMENT2) analysis were frozen, lyophilized, and dissolved in aqua regia, prepared by adding 100 μL of nitric acid + 300 μL of 37% hydrochloric acid for 72 h to dissolve gold particles. Then, samples were diluted to 10 mL with 9.6-mL 2% HNO_3 and analyzed via ICP-MS against standards. Control saline and organ samples with exogenously added PEG-NRs were used to calibrate this method.

***In vivo* circulation time and biodistribution of PEG-NRs.** Nude mice were bilaterally injected s.c. in the hind flank with ~2 × 10^6 MDA-MB-435 cells. After 2 to 3 wk, animals were anaesthetized with isoflurane and injected through the tail vein with PEG-NRs in 0.15 mol/L NaCl, 0.1 mol/L Na phosphate buffer (pH 7.2; 20 mg Au/kg). 10 μL blood samples were withdrawn periodically from the suborbital space, diluted with PBS containing 10 mmol/L EDTA, centrifuged to remove RBCs, and read on a spectrophotometer to assess PEG-NR plasmon peak height. For biodistribution experiments, after vascular clearance of PEG-NRs (72 h), injected animals were euthanized and organs were collected, weighed, and lyophilized for ICP-MS quantification of PEG-NR biodistribution.

***In vivo* photothermal heating of gold NRs and photothermal therapy.** For both initial modeling and growth curve assessments after photothermal treatment, nude mice were bilaterally injected in the hind flank with ~2 × 10^6 MDA-MB-435 cells. After 2 to 3 wk, animals were anaesthetized with isoflurane and injected through the tail vein with PEG-NRs in PBS (20 mg Au/kg) or PBS alone. After vascular clearance of PEG-NRs (72 h), the right flank of each mouse was irradiated (2 W/cm^2, 810 nm, 1 cm beam diameter). Thermographic imaging of photothermal heating was used to facilitate modeling of three-dimensional temperature distributions in tumors (n = 3 mice for each set). To explore the hematologic effects of NR administration and near-IR ablation, mice bearing bilateral MDA-MB-435 tumors were injected with saline or PEG-NRs and, 72 h later, either exposed to the therapeutic tumor irradiation protocol under anesthesia (~2 W/cm^2, 5 min, 810 nm) or anesthesia without irradiation (n = 3 each set). After exposure, blood was collected for hematology and mice were sacrificed. Therapeutic assessment of the affect of PEG-NR heating on tumor growth was conducted similarly (n = 4 mice in each treatment set). Both irradiated and unirradiated tumors of each mouse in the therapeutic assessment trial

Published OnlineFirst April 14, 2009; DOI: 10.1158/0008-5472.CAN-08-4242

were measured at regular intervals using digital calipers. Survival studies were conducted using mice that were unilaterally injected in the hind flank with $\sim 2 \times 10^6$ MDA-MB-435 cells (n = 5 mice in each treatment set). Tumor sizes were measured over time, and mice were euthanized once tumors exceeded 500 mm^3.

Results

Development of ultrastable, polymer-coated gold NRs. In principle, gold nanoparticles are attractive for medical applications because various formulations have been approved by the U.S. Food and Drug Administration and in clinical use for decades. However, one barrier facing the widespread biological use of gold NRs has been the need to replace the cationic CTAB surfactants used to drive their anisotropic growth with hydrophilic, biocompatible coatings. We found that NRs, with axial sizes of 12.7 nm (±3.4) and 47 nm (±9.3; Fig. 1*A*), coated in CTAB are cytotoxic and colloidally unstable in 0.15 mol/L NaCl or 10% human serum (Fig. 1*B* and *C*). After PEGylation (Fig. 1*B*), gold NRs contained ~20,000 polymers per particle by the SPDP assay (25) and were rendered highly stable *in vitro*, showing minimal spectral shifting (which would indicate particle destabilization and aggregation) even after >1,000 hours in 0.15 mol/L NaCl or 10% human serum (Fig. 1*C* and Supplementary Fig. S1*A*). Additionally, PEG-NRs could be dispersed in a variety of solvents, including acetone, acetonitrile, DMSO, DMF, ethanol, and methanol, further highlighting the stability of their coating and their amenability to future chemical processing and functionalization (Supplementary Fig. S1*B*). After 24 hours of incubation above primary rat hepatocyte cocultures, an *in vitro* liver model that was previously used to elucidate semiconductor quantum dot toxicity (26) and has shown utility for rank-ordering pharmacologic toxicities (27), PEG-NRs, displayed no significant alterations in mitochondrial activity compared with saline alone, even at doses 20 times greater than that used over cells *in vitro* here and equal to maximal blood concentrations during *in vivo* therapy experiments (Supplementary Fig. S2), highlighting their potential biocompatibility for medical applications.

Photothermal comparison of gold NRs and gold nanoshells. In light of the prior utility of gold nanoshells for photothermal tumor therapy, they were used as a benchmark here to evaluate the photothermal performance of PEG-NRs (Fig. 2*A*): PEGylated nanoshell preparations with similar composition and spectra to those used for photothermal *in vivo* applications (refs. 5, 6, 9; ~120 nm silica cores and ~15 nm gold shells, 810 nm peak plasmon resonance; Fig. 2*B*). PEG-NRs exhibited <1/3 of the spectral bandwidth and ~3 times higher extinction coefficient per gram gold than PEG-nanoshells (full width at half maximum of PEG-NRs 130 nm, PEG-nanoshells 490 nm; Fig. 2*B*). Additionally, under identical experimental conditions, irradiated PEG-NR solutions generated heat >6 times more rapidly than PEG-nanoshells per gram gold (Fig. 2*C*). These findings are consistent with theoretical calculations indicating that gold NRs of this size exhibit superior per micron absorption coefficients to gold nanoshells (14). Accordingly, incubation of PEG-NRs with MDA-MB-435 human tumor cells *in vitro* enabled their widespread destruction with levels of NIR light that were insufficient for nanoshell-mediated toxicity (Fig. 2*D*). Exposure to individual stimuli (NRs, nanoshells, or laser) did not affect cell viability (Supplementary Fig. S3).

X-ray CT and computational modeling of photothermal NR heating *in vivo*. To translate the photothermal efficacy of PEG-NRs to *in vivo* therapy, we next developed a method through which PEG-NRs could be heated under the guidance of biodistribution-based computational photothermal modeling. To model and customize patient irradiation regimens, we sought to acquire

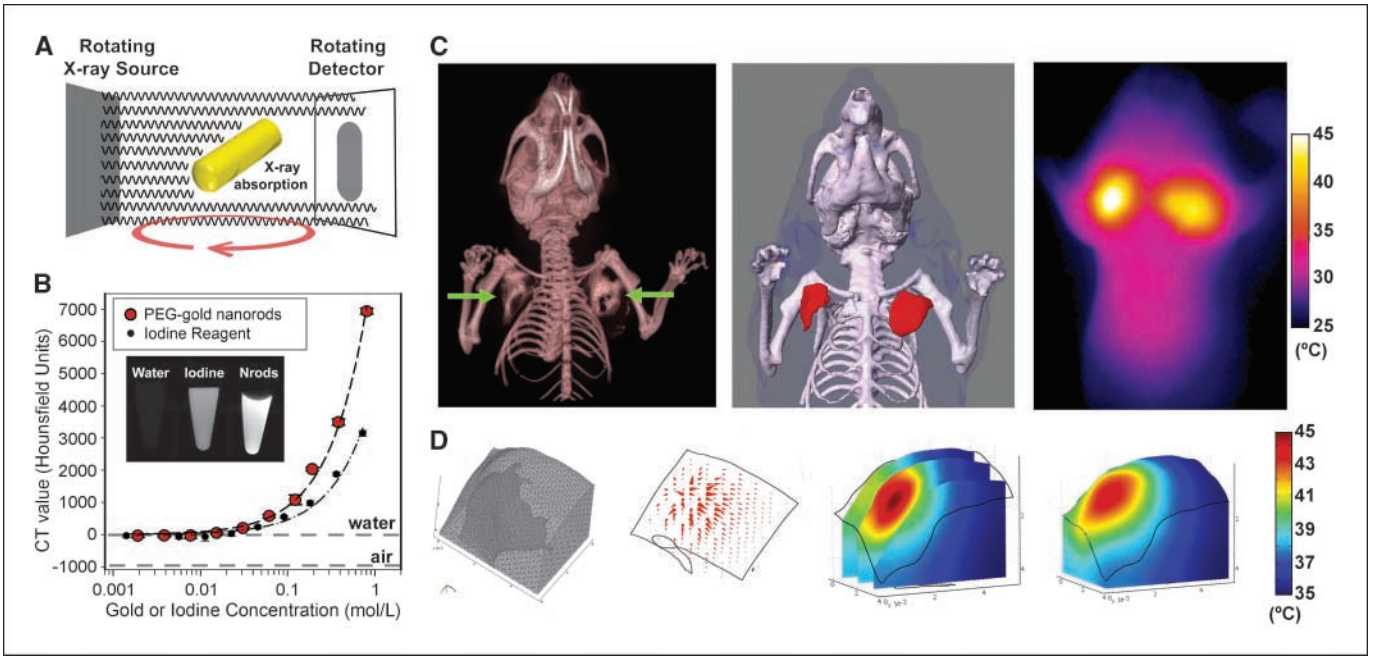

Figure 3. X-ray CT, quantitative photothermal modeling, and near-IR photothermal heating of gold NRs *in vivo*. *A,* schematic of X-ray absorption by gold NRs in X-ray CT. *B,* X-ray CT number of PEG-NRs compared with an iodine standard (Isovue-370). *C,* PEG-NRs were intratumorally given to mice bearing bilateral MDA-MB-435 tumors and imaged using X-ray CT to visualize three-dimensional PEG-NR distribution in tumors (*left*). A three-dimensional solid model of the complete geometry was rapidly reconstructed by image processing for use with computational photothermal modeling (*middle*). *Red,* PEG-NRs. Experimental thermographic surveillance of NIR irradiation after X-ray CT (~0.75 W/cm^2, 1 min; *right*). *D,* meshed geometry of the left tumor chosen as the computational domain (*left*). Plot of theoretical heat flux propagation inside the tumor upon irradiation (*middle left*). Predicted internal temperature distribution at three different planes inside the tumor (*middle right*) along with surface temperature map (*right*) matching the left tumor in *C*.

Published OnlineFirst April 14, 2009; DOI: 10.1158/0008-5472.CAN-08-4242

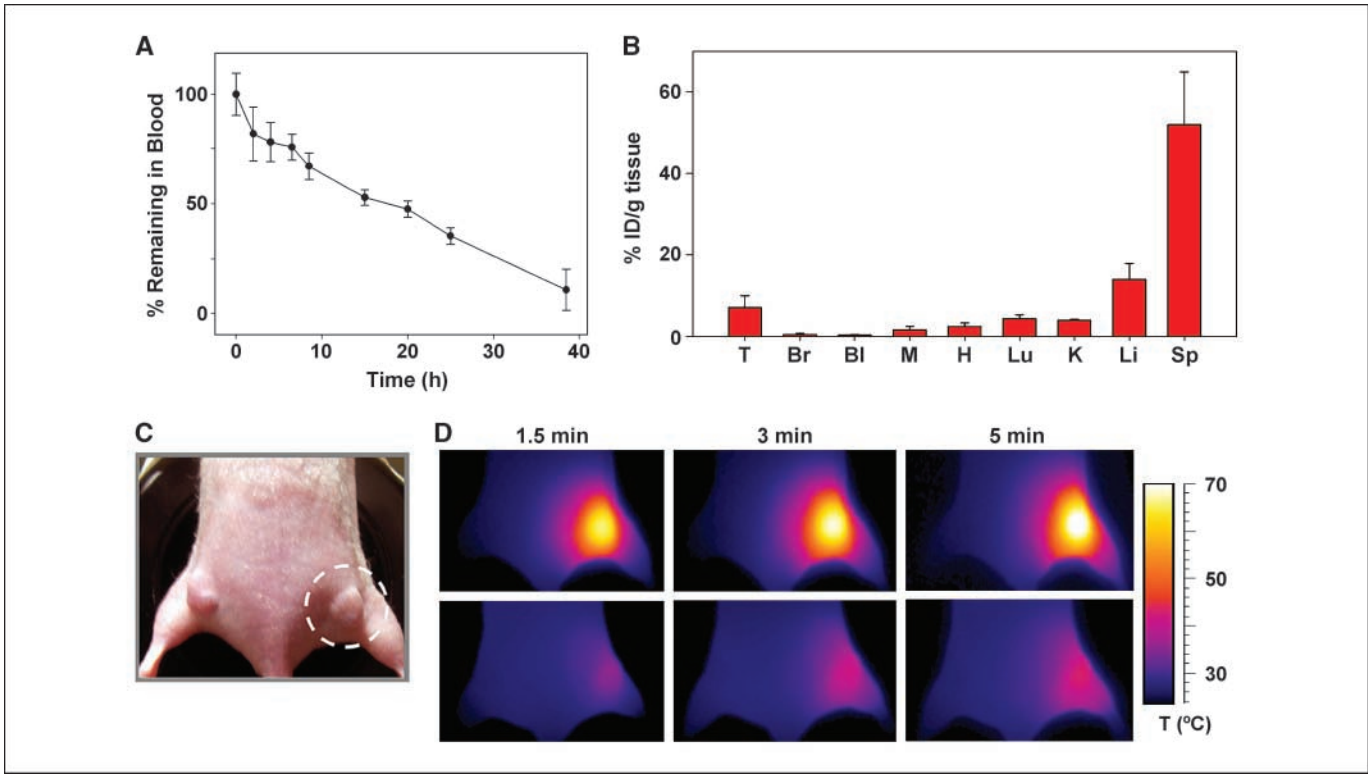

Figure 4. Long circulation time, passive tumor targeting, and photothermal heating of passively targeted gold NR antennas in tumors. *A,* PEG-NRs were i.v. given (20 mg/kg) to three mice bearing MDA-MB-435 tumors, and blood was withdrawn over time to monitor clearance from circulation. *B,* PEG-NR biodistribution and targeting to MDA-MB-435 tumors 72 h after i.v. administration, quantified via ICP-MS (three mice). *T,* tumor; *Br,* brain; *Bl,* bladder; *M,* muscle; *H,* heart; *Lu,* lung; *K,* kidney; *Li,* liver; *SP,* spleen. Data are tabulated in Supplementary Table S1. *C,* PEG-NRs or saline were i.v. given (20 mg/kg) to mice bearing MDA-MB-435 tumors on opposing flanks. After NRs had cleared from circulation (72 h after injection), the right flank was irradiated using an 810-nm diode laser (2 W/cm^2; beam size indicated by dotted circle). *D,* thermographic surveillance of photothermal heating in PEG-NR–injected (*top*) and saline-injected (*bottom*) mice.

nanoparticle distributions remotely using X-ray CT, a desirable imaging modality due to its high three-dimensional anatomic resolution, rapid imaging speed, quantitative dynamic range of detection, full body penetration, and ubiquitous clinical use. To investigate the ability of PEG-NRs to act as dense X-ray absorbing agents for X-ray CT, solutions of PEG-NRs were serially diluted and imaged using a GE microCT scanner (Fig. 3*A*). The resulting relationship between PEG-NR concentration and X-ray contrast was highly linear and exhibited ~2-fold amplified X-ray contrast compared with a clinical iodine standard per mole (Fig. 3*B* and Supplementary Fig. S4), analogous to that found previously for spherical gold nanoparticle reagents (21, 22). In addition to providing enhanced X-ray absorption, PEG-NRs allow NIR photothermal heating whereas iodine reagents show no heating above water alone (Supplementary Fig. S4).

To assess the utility of the high X-ray absorption of PEG-NRs for remote detection *in vivo*, ~3 pmol of PEG-NRs (~1 μmol Au) were directly injected into the tumors of mice bearing bilateral human MDA-MB-435 tumors, implanted either in the mammary fat pad or the rear flank. We found that X-ray CT rapidly detailed the three-dimensional distribution of PEG-NRs in tumors, showing clear distinction between NRs and soft tissues (Fig. 3*C* and Supplementary Figs. S5 and S6). To understand the relationship between the nanoparticle distribution in tumors and the associated processes of thermal deposition and flux during irradiation, a finite element model of PEG-NR heating was developed based on the Pennes bioheat transfer equation, including (*a*) three-dimensional skeletal, soft tissue, and PEG-NR geometries transferred from X-ray CT imaging; (*b*) temperature-dependent optical absorption and scattering; (*c*) heat transfer, including surface thermal flux, internal diffusive flux, and temperature-dependent perfusive thermal flux in tissues; and (*d*) an extracorporeal NIR laser of variable intensity, beam diameter, and orientation matching used (see supplementary data). X-ray CT data was exported into ScanIP and ScanFE image processing software for skeletal, NR, and soft tissue geometry construction and subsequently into COMSOL Multiphysics modeling software for photothermal simulations. Exported geometries enabled rapid delineation PEG-NRs, along with skeletal structures and surrounding soft tissues for spatially defining model parameters (Fig. 3*C* and Supplementary Figs. S5 and S6). Computational, finite element heat transfer simulations were performed using PEG-NRs and tumor geometries as computational domains to evaluate the feasibility of applying four-dimensional modeling to the process of photothermal heating under irradiation (Fig. 3*D* and Supplementary Fig. S6). Simulations revealed the intratumoral vectors of thermal flux extending from regions of PEG-NRs, as well as the internal and surface temperature history expected for irradiation at varying laser intensities (Fig. 3*D* and Supplementary Fig. S6). At matched computational and experimental laser intensities, simulated surface heating behavior qualitatively and quantitatively matched the observed surface temperature values and distributions acquired using IR thermographic observation (Fig. 3*D* and Supplementary Fig. S6). We believe this establishes the potential of fusing quantitative imaging with computational

Published OnlineFirst April 14, 2009; DOI: 10.1158/0008-5472.CAN-08-4242

modeling to provide insight into the unintuitive, highly complex phenomena of *in vivo* photothermal heating. Next, we proceeded to explore the power of this modeling to quantitatively predict *in vivo* heating after i.v. tumor targeting.

Long circulation time and photothermal tumor heating after i.v. NR administration. We next investigated the behavior of PEG-NRs after i.v. administration in mice to systemically target tumors through the enhanced permeability and retention effect (28). For PEG-NRs to passively target tumors via the enhanced permeability and retention effect and act as nanoantennas for photothermal therapy, they must be able to traverse the systemic circulation, deter protein opsonization and reticuloendothelial system (RES) clearance, permeate through transendothelial pores in tumor blood vessels, and be retained in the tumor interstitium. After i.v. administration to tumor-bearing mice (20 mg Au/kg), our PEG-NRs were found to exhibit blood half-lives of ~17 hours (Fig. 4*A*) and to maintain their 810-nm longitudinal plasmon resonance throughout this time, allowing spectrophotometric detection in serum over time (Supplementary Fig. S7).

To quantitatively assess tumor accumulation of PEG-NRs, nude mice bearing MDA-MB-435 human tumors were given i.v. PEG-NRs, and once NRs had cleared from circulation (72 hours), organs were removed for gold quantitation. Here, ICP-MS was used to quantify the accumulation of exogenously given gold in tissues. ICP-MS Au NR detection was found to be highly sensitive and linear across a relevant range for gold NR detection (Supplementary Fig. S8). As expected for nanomaterials above the renal filtration limit, PEG-NRs were found to clear via RES uptake with splenic clearance dominating hepatic (Fig. 4*B*; Supplementary Table S1), a pattern analogous to that observed previously for PEG-protected 10-nm diameter spherical gold nanoparticles (21). Importantly, passive tumor accumulation of PEG-NRs after injection was found to be highly efficient, even at 72 hours after injection, accumulating at ~7% ID/g (Fig. 4*B*; Supplementary Table S1), allowing PEG-NRs to amplify the tumor absorption coefficient of 810 nm light by ~7 fold (see supplementary data). Based on empirical studies of passive tumor targeting, the enhancement of the PEG-NR circulation time over reported PEG-nanoshell formulations should amplify their passive tumor accumulation in tumors, which, in concert with their enhanced photothermal heat generation *in vitro*, would be expected to provide overall enhanced photothermal contrast between tumors and normal tissue. However, as PEG-nanoshells are not commercially available, a side-by-side *in vivo* comparison could not be pursued. Separately, to study the long-term clearance of PEG-NRs from RES organs, tumor-free mice were injected with PEG-NRs and sacrificed 2 months after injection. During these 2 months, injected mice showed no signs over NR toxicity, such as weakness, belabored breathing, or failure to thrive. Organ analysis showed that the %ID/g values for tissues decreased by >50% in all organs and by >80% in muscle, heart, lungs, and kidneys (Supplementary Fig. S9), indicating the existence of routes for gold NR clearance after uptake in tissues.

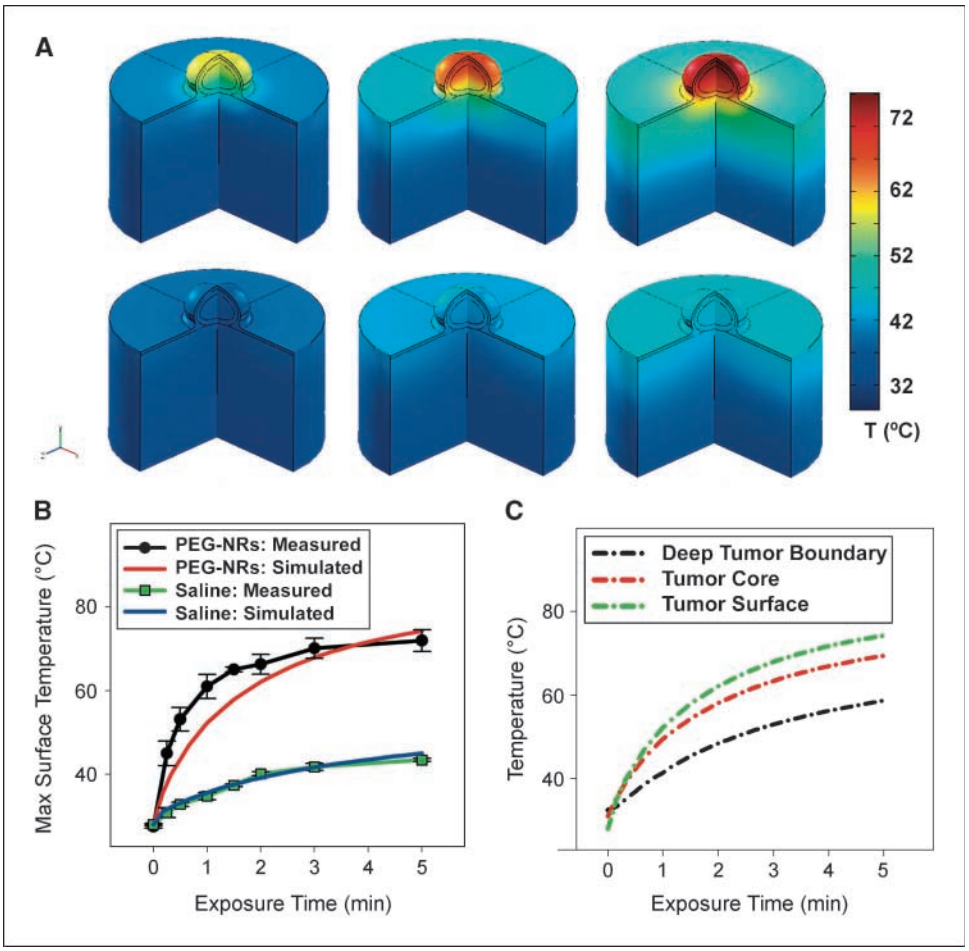

Figure 5. Quantitative photothermal modeling of gold NR tumor heating. *A,* three-dimensional finite element modeling of PEG-NR heating *in vivo*. Simulated three-dimensional temperature distributions matching the four-dimensional thermographic time points for PEG-NR (*top*) and control tumor irradiation (*bottom*). *B,* thermographically measured and simulated tumor surface temperatures over time for irradiation of PEG-NR or saline mice. *C,* simulated temperature increases various depths for PEG-NR–injected and saline-injected mice. By 5 min after the onset of irradiation, the entire PEG-NR tumor is predicted to have reached ablative temperatures of >60°C, motivating the choice of this irradiation regimen for subsequent therapeutic trials.

Published OnlineFirst April 14, 2009; DOI: 10.1158/0008-5472.CAN-08-4242

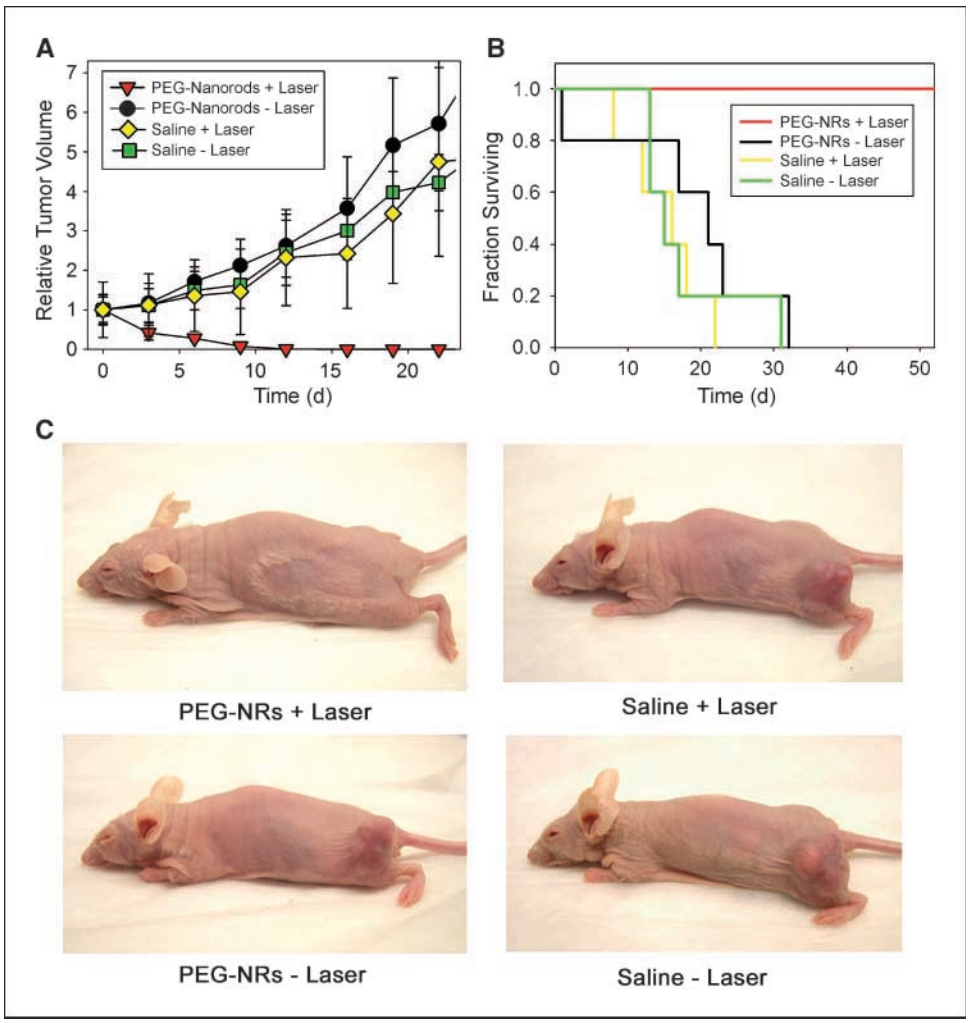

Figure 6. Photothermal destruction of human tumors in mice using long-circulating gold NRs. *A,* mice harboring two MDA-MB-435 human tumors on opposite flanks were injected with either saline or PEG-NRs. After PEG-NRs had cleared from circulation (72 h after injection), the right flank of each mouse was exposed to the computationally designed irradiation regimen (810 nm, 2 W/cm^2, 5 min). Volumetric changes in tumor sizes are plotted over time after irradiation. *B,* mice harboring one MDA-MB-435 human tumor were injected with either saline or PEG-NRs and irradiated as in *A*. Survival of mice after irradiation is plotted versus time after irradiation. *C,* at 20 d after irradiation, NIR-irradiated, all PEG-NR–injected mice showed only a minor scar and no evidence of tumor regrowth whereas all other treatment groups harbored thriving tumors.

Having observed their efficient passive homing to human tumors via the enhanced permeability and retention effect, the ability of PEG-NRs to remain active as optical nanoantennas for photothermal tumor heating after clearance from the systemic circulation (~72 hours) was subsequently investigated. Either PEG-NRs (20 mg Au/kg) or a saline solution was given i.v. into mice bearing two MDA-MB-435 tumors on opposite flanks. Once PEG-NRs had cleared from circulation (72 hours), irradiated tumors on PEG-NR–injected mice rapidly heated to temperatures of over 70°C (Fig. 4*C*), whereas saline-injected mice displayed less focal temperature increases with maximum surface temperatures of ~40°C (Fig. 4*D*). To inform the development of near-IR radiation doses that would fully destroy tumors, photothermal heating simulations were again conducted using the i.v. biodistribution data and computational domains containing ellipsoidal tumor geometries matching those used in experiments (Supplementary Fig. S10). Photothermal heating simulations closely matched experimental surface temperature data (Figs. 4*D* and 5*A* and *B*), suggesting that tumor-targeted nanoantennas substantially retained their photothermal efficacy during the 72 hours after injection *in vivo*. Furthermore, the simulations predicted that the entire tumor volume, including the deepest tumor/tissue interface, would be heated to ablative temperatures (>60°C) by 5 minutes after the onset of laser irradiation (Fig. 5*C*). Thus, a 5-minute, 2-W/cm^2 irradiation regimen was used for subsequent therapeutic experiments in an effort to provide fully destructive photothermal tumor treatment.

Photothermal tumor destruction using a computationally designed irradiation regimen. To test the prediction that a single dose of PEG-NRs could destroy tumors under the computationally designed protocol of NIR irradiation, nude mice bearing bilateral human MDA-MB-435 tumors were injected with either PEG-NRs or saline. After i.v. clearance of PEG-NRs, the right flank of each mouse was irradiated for 5 min (810 nm, 2 W/cm^2) and all tumors were measured at regular intervals over time. Within 10 days all the irradiated, PEG-NR–targeted tumors completely disappeared by external observation whereas all other tumors, including those exposed to laser after saline injection, continued to grow uninhibited (Fig. 6*A*). To assess the survival benefit of PEG-NR–directed tumor ablation, mice bearing a single MDA-MB-435 tumor were divided between four cohorts (PEG-NRs + laser, PEG-NRs − laser, saline + laser, saline − laser) and all tumors were measured over time (Fig. 6*B*). By 20 days after treatment, all irradiated, PEG-NR–injected mice displayed only a minor scar with no evidence of tumor regrowth, whereas all other surviving mice harbored thriving tumors (Fig. 6*B* and *C*). Over the course of >50 days of observation, no irradiated, PEG-NR–injected mice showed evidence of recurrence whereas all mice in the control had to be euthanized by day 33.

Published OnlineFirst April 14, 2009; DOI: 10.1158/0008-5472.CAN-08-4242

Body weights of PEG-NR–treated mice were monitored over time and showed no obvious losses due to tumor ablation and resorption (Supplementary Fig. S11). In a separate experiment to assess the acute hematologic effects of NR-directed tumor ablation, the only statistically significant change observed in response to NR-mediated tumor ablation was a slight increase in the percentage of band neutrophils in NR + laser sets ($P < 0.05$ for NR+ laser versus NR, saline + laser, and saline; Supplementary Fig. S12), likely due to an acute inflammatory response to tumor ablation.

Discussion

Here, we present the development of an integrated system for nanoantenna-based photothermal tumor therapy involving the synthesis of long-circulating gold NRs as efficient NIR-nanoantennas, biodistribution data acquisition via X-ray CT nanomaterial imaging or *ex vivo* spectrometry, and photothermal computational modeling to guide surgical irradiation planning. Broadly, the efficacy of a nanoantenna for photothermal therapy depends on both intrinsic (optical absorption coefficient and material cytotoxicity) and extrinsic (polymer coating, macrophage affinity, and circulation time) material characteristics, as well as external parameters, such as the use of optimized dosing and irradiation protocols for effective treatment.

We show that PEG-NRs exhibit superior intrinsic absorption and photothermal efficacy compared with gold nanoshells (~6 times greater heat generation per weight gold), as well as substantially improved circulation times *in vivo* (~17 hours versus ~4 hours), extrinsically imparted by their polymer coating (5, 6). Surveying literature on inorganic nanoparticle circulation times *in vivo*, the circulation half-life of PEG-NRs is among the longest achieved to date. Previously, polymer-stabilized inorganic nanomaterials have been described with circulation half-lives of a few hours *in vivo* (29, 30), including a variety of other gold nanoparticle preparations (22, 31–33), and on occasion with circulation times of ~10 to 15 hours in mice (21, 28, 34). Elsewhere, another PEG-NR formulation was developed for *in vivo* applications, but showed a 30-minute half-life without investigation into their ability to passively target tumors or mediate *in vivo* photothermal heating (32). Because nanoparticle circulation time has been shown to determine the efficiency of nanoparticle accumulation in tumors via the enhanced permeability and retention effect, in mouse cancer models and clinical cancer treatment (28), the long circulation time reported here has the potential to directly translate to improved clinical tumor accumulation over previous nanoantennas.

Beyond the material determinants of nanoantenna efficacy, the irradiation protocol used (i.e., beam intensity, shape, cross-section, duration, direction, etc.) and nanoantenna dosing regimen directly control the rates of energy capture and dissipation to surrounding tissues *in vivo*. Whereas nanoantennas have the potential to increase the selectivity of tumor ablation, unoptimized irradiation of tissues carries the risks of either unnecessary morbidity due to collateral damage or ineffective therapy due to incomplete treatment of tumor margins. Here, we show that quantitative biodistribution data incorporated into computational modeling can help anticipate the photothermal heating in tumors and surrounding tissues during irradiation. Future developments of the quantitative model presented here could enable rapid quantitative modeling of photothermal temperature gradients in arbitrarily complex three-dimensional tissues and provide a route toward *a priori* personalization of irradiation regimens. As a proof of principle, we establish a means of integrating whole-subject X-ray CT data with quantitative heat transfer modeling, offering a new route toward merging the clinical paradigms of imaging and therapy for personalized four-dimensional radiation planning and optimization. Furthermore, using a computationally planned therapeutic method, we show that i.v. administration of PEG-NR nanoantennas enabled complete destruction of all irradiated tumors under otherwise benign near-IR light.

We believe our findings motivate future investigation into the long-term biodistribution of PEG-NRs, more extensive analysis of their potential toxicity *in vivo*, and the development of methods for detecting low concentrations of PEG-NRs in whole animals to remotely quantify i.v. tumor targeting. Methods for actively targeting NRs to tumors, particularly to vascular epitopes, could potentially enhance their specificity for tumors or direct their additional accumulation in premalignant lesions and metastatic lymphatics. Finally, we provide clear evidence that the application of quantitative biodistribution-based modeling to the *in vivo* testing of nanomaterials can provide insight into their function and direct procedural optimization.

Disclosure of Potential Conflicts of Interest

G. von Maltzahn: Consultant and ownership interest, Concurrent Analytical. The other authors declared no potential conflicts of interest.

Acknowledgments

Received 11/5/08; revised 2/5/09; accepted 2/5/09; published OnlineFirst 4/14/09.

Grant support: NIH grant BRP R01CA124427-01, NIH/National Cancer Institute grants U54 CA119349 and U54 CA119335, Packard Fellowship (1999-1453), and Whitaker Foundation and National Science Foundation (G. von Maltzahn).

The costs of publication of this article were defrayed in part by the payment of page charges. This article must therefore be hereby marked *advertisement* in accordance with 18 U.S.C. Section 1734 solely to indicate this fact.

We thank Dr. Shelley J. Coldiron and Dr. Christian Schoen at Nanopartz for developing the CTAB nanorods used in this work, Dr. Yoel Fink for generously lending the FLIR IR thermographic camera, and Dr. Eugene Zubarev and Bishnu Khanal at Rice University for their synthesis and characterization of CTAB-coated gold nanorods through Nanopartz.

References

1. Elghanian R, Storhoff JJ, Mucic RC, Letsinger RL, Mirkin CA. Selective colorimetric detection of polynucleotides based on the distance-dependent optical properties of gold nanoparticles. Science 1997;277:1078–81.
2. Grubisha DS, Lipert RJ, Park HY, Driskell J, Porter MD. Femtomolar detection of prostate-specific antigen: an immunoassay based on surface-enhanced Raman scattering and immunogold labels. Anal Chem 2003;75:5936–43.
3. Jackson JB, Westcott SL, Hirsch LR, West JL, Halas NJ. Controlling the surface enhanced Raman effect via the nanoshell geometry. Appl Phys Lett 2003;82:257–9.
4. Qian XM, Peng XH, Ansari DO, et al. *In vivo* tumor targeting and spectroscopic detection with surface-enhanced Raman nanoparticle tags. Nat Biotechnol 2008;26:83–90.
5. Hirsch LR, Stafford RJ, Bankson JA, et al. Nanoshell-mediated near-infrared thermal therapy of tumors under magnetic resonance guidance. P Natl Acad Sci USA 2003;100:13549–54.
6. O'Neal DP, Hirsch LR, Halas NJ, Payne JD, West JL. Photo-thermal tumor ablation in mice using near infrared-absorbing nanoparticles. Cancer Lett 2004;209:171–6.
7. Norman RS, Stone JW, Gole A, Murphy CJ, Sabo-Attwood TL. Targeted photothermal lysis of the pathogenic bacteria, *Pseudomonas aeruginosa*, with gold nanorods. Nano Lett 2008;8:302–6.
8. Huang X, El-Sayed IH, Qian W, El-Sayed MA. Cancer cell imaging and photothermal therapy in the near-infrared region by using gold nanorods. J Am Chem Soc 2006;128:2115–20.

Published OnlineFirst April 14, 2009; DOI: 10.1158/0008-5472.CAN-08-4242

9. Gobin AM, Lee MH, Halas NJ, James WD, Drezek RA, West JL. Near-infrared resonant nanoshells for combined optical imaging and photothermal cancer therapy. Nano Lett 2007;7:1929–34.

10. Xie H, Gill-Sharp KL, O'Neal P. Quantitative estimation of gold nanoshell concentrations in whole blood using dynamic light scattering. Nanomed Nanotechnol 2007;3:89–94.

11. James WD, Hirsch LR, West JL, O'Neal PD, Payne JD. Application of INAA to the build-up and clearance of gold nanoshells in clinical studies in mice. J Radioanal Nucl Ch 2007;271:455–9.

12. Dickerson EB, Dreaden EC, Huang X, et al. Gold nanorod assisted near-infrared plasmonic photothermal therapy (PPTT) of squamous cell carcinoma in mice. Cancer Lett 2008;269:57–66.

13. Murphy CJ, San TK, Gole AM, et al. Anisotropic metal nanoparticles: synthesis, assembly, and optical applications. J Phys Chem B 2005;109:13857–70.

14. Jain PK, Lee KS, El-Sayed IH, El-Sayed MA. Calculated absorption and scattering properties of gold nanoparticles of different size, shape, and composition: applications in biological imaging and biomedicine. J Phys Chem B 2006;110:7238–48.

15. Hu M, Chen JY, Li ZY, et al. Gold nanostructures: engineering their plasmonic properties for biomedical applications. Chem Soc Rev 2006;35:1084–94.

16. Yu C, Nakshatri H, Irudayaraj J. Identity profiling of cell surface markers by multiplex gold nanorod probes. Nano Lett 2007;7:2300–6.

17. Wang H, Huff TB, Zweifel DA, et al. *In vitro* and *in vivo* two-photon luminescence imaging of single gold nanorods. Proc Natl Acad Sci U S A 2005;102:15752–6.

18. Skirtach AG, Karageorgiev P, De Geest BG, Pazos-Perez N, Braun D, Sukhorukov GB. Nanorods as wavelength-selective absorption centers in the visible and near-infrared regions of the electromagnetic spectrum. Adv Mater 2008;20:506–10.

19. Tong L, Zhao Y, Huff TB, Hansen MN, Wei A, Cheng JX. Gold nanorods mediate tumor cell death by compromising membrane integrity. Adv Mater 2007;19:3136–41.

20. Huff TB, Tong L, Zhao Y, Hansen MN, Cheng JX, Wei A. Hyperthermic effects of gold nanorods on tumor cells. Nanomedicine-UK 2007;2:125–32.

21. Cai QY, Kim SH, Choi KS, et al. Colloidal gold nanoparticles as a blood-pool contrast agent for X-ray computed tomography in mice. Invest Radiol 2007;42:797–806.

22. Kim D, Park S, Lee JH, Jeong YY, Jon S. Antibiofouling polymer-coated gold nanoparticles as a contrast agent for *in vivo* X-ray computed tomography imaging. J Am Chem Soc 2007;129:7661–5.

23. Harris JM, Chess RB. Effect of pegylation on pharmaceuticals. Nat Rev Drug Discov 2003;2:214–21.

24. Duncan R. The dawning era of polymer therapeutics. Nat Rev Drug Discov 2003;2:347–60.

25. Josephson L, Tung CH, Moore A, Weissleder R. High-efficiency intracellular magnetic labeling with novel superparamagnetic-tat peptide conjugates. Bioconjug Chem 1999;10:186–91.

26. Derfus AM, Chan WCW, Bhatia SN. Probing the cytotoxicity of semiconductor quantum dots. Nano Lett 2004;4:11–8.

27. Khetani SR, Bhatia SN. Microscale culture of human liver cells for drug development. Nat Biotechnol 2008;26:120–6.

28. Moghimi SM, Hunter AC, Murray JC. Long-circulating and target-specific nanoparticles: theory to practice. Pharmacol Rev 2001;53:283–318.

29. Ballou B, Lagerholm BC, Ernst LA, Bruchez MP, Waggoner AS. Noninvasive imaging of quantum dots in mice. Bioconjug Chem 2004;15:79–86.

30. Rabin O, Perez JM, Grimm J, Wojtkiewicz G, Weissleder R. An X-ray computed tomography imaging agent based on long-circulating bismuth sulphide nanoparticles. Nat Mater 2006;5:118–22.

31. Paciotti GF, Myer L, Weinreich D, et al. Colloidal gold: a novel nanoparticle vector for tumor directed drug delivery. Drug Deliv 2004;11:169–83.

32. Niidome T, Yamagata M, Okamoto Y, et al. PEG-modified gold nanorods with a stealth character for *in vivo* applications. J Control Release 2006;114:343–7.

33. Qian X, Peng XH, Ansari DO, et al. *In vivo* tumor targeting and spectroscopic detection with surface-enhanced Raman nanoparticle tags. Nat Biotechnol 2008;26:83–90.

34. Weissleder R, Bogdanov A, Neuwelt EA, Papisov M. Long-circulating iron-oxides for MR-imaging. Adv Drug Deliver Rev 1995;16:321–34.

Supporting Information Available.

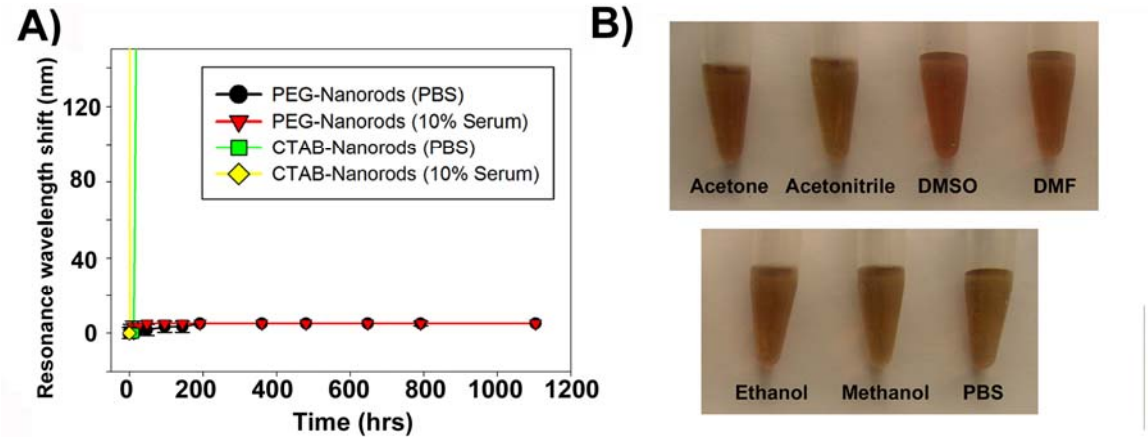

Supplementary Figure 1: *PEG-Nanorod Synthesis and Stability In Vitro.* A) The plasmon resonance of gold nanomaterials is highly sensitive to aggregation-mediated red-shifting. By monitoring plasmon resonance peak over >1000 hrs in biological solutions, we find that PEG-nanorods show prolonged stability in biological media while CTAB-coated nanorods aggregated over time in PBS (0.15 M NaCl 0.1 M Na Phosphate, pH 7.2) or 10% human serum monitored for over 1000 hrs *in vitro*. B) PEG-NRs were readily dispersed in a variety of solvents, including acetone, acetonitrile, dimethyl sulfoxide (DMSO), dimethylformamide (DMF), ethanol, methanol, or PBS.

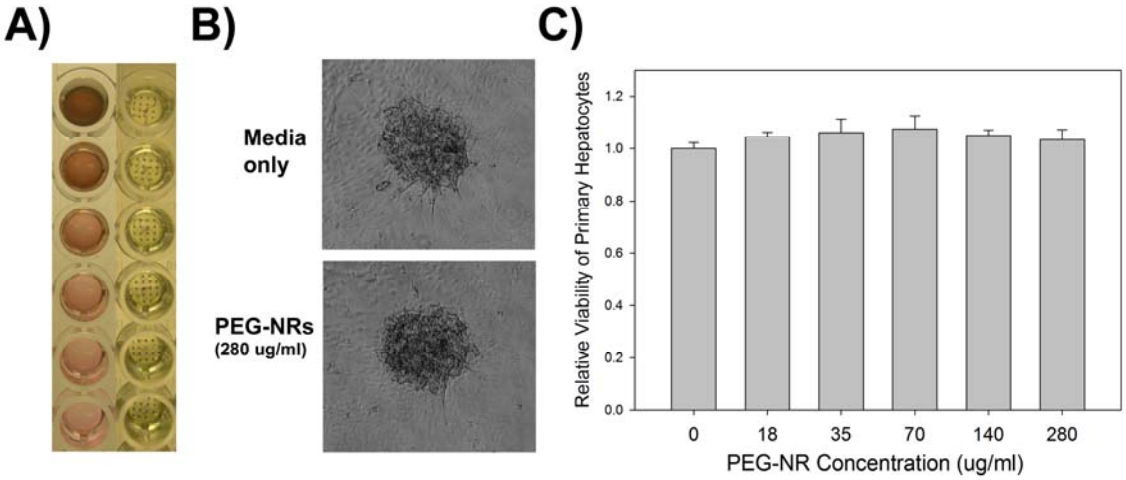

Supplementary Figure 2: *Probing Nanorod Cytotoxicity to Primary Rat Hepatocyte cocultures.* A) Primary rat hepatocyte: 3T3-J2 human fibroblast co-cultures were incubated with PEG-NRs at varying concentrations for 24 hrs (left column), rinsed, and incubated with media containing thiazolyl blue tetrazolium bromide (MTT reagent) at 0.5 mg/ml. After 1hr, blue precipitates begin to form within hepatocytes as a result of mitochondrial activity (right column). B) Microscopy shows cultures incubated with PEG-NRs at maximal concentrations to show similar morphology to controls. C) Quantitaion of cellular viability via absorbance of DMSO:isopropanol-solubilized MTT reagent shows no cytotoxicity of PEG-NRs, even at concentrations of 20-times that used *in vitro* here and approximately equal to maximum blood concentrations during *in vivo* experiments.

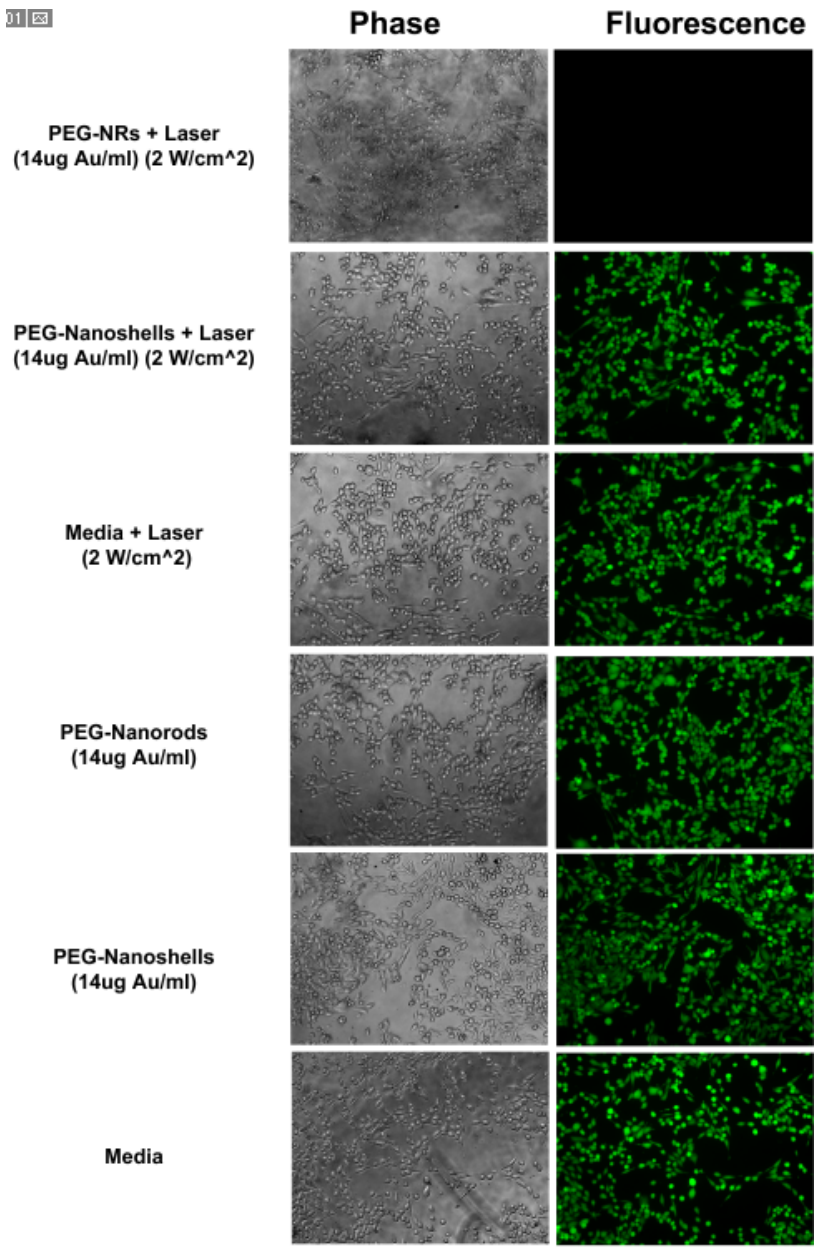

Supplementary Figure 3: *Probing Photothermal PEG-Nanorod Cytotoxicity to MDA-MB-435 Tumor Cell Cultures Compared to PEG-Nanoshells.* Human tumor cell cultures (MDA-MB-435) were incubated with PEG-Nanorods (14 μg/ml), PEG-Nanoshells (14 μg/ml), or media and irradiated at 2 W/cm^2 for 5 min. Following irradiation, cells were washed and incubated with Calcein AM, a fluorogenic esterase substrate, to detect cell viability. Irradiation of PEG-Nanorods leads to photothermal destruction of cells, while controls and PEG-Nanoshells show high cell viability.

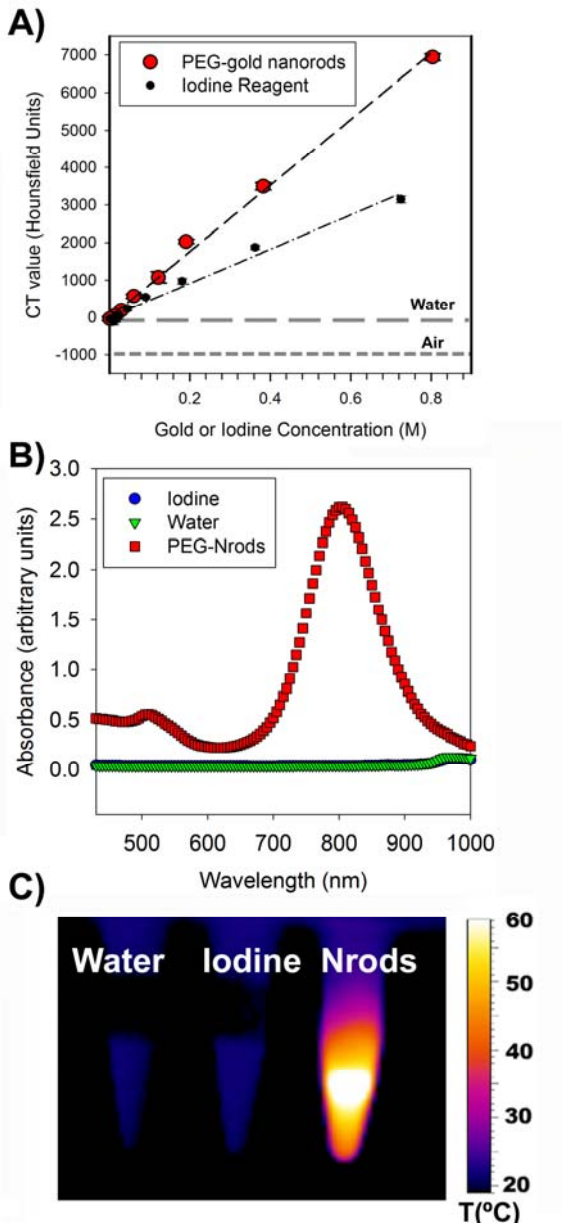

Supplementary Figure 4: *X-ray Absorption, Optical Spectra, and Photothermal Comparison between PEG-Nanorods and Clinical Iodine X-ray Computed Tomography Reagent.* A) X-ray computed tomography number of PEG-nanorods compared to an iodine standard (Isovue-370). Linear x-axis plot of the same data presented in Figure 2B, clarifying linearity of PEG-gold nanorod detection via x-ray CT B) Optical extinction spectra of PEG- Nanorods (0.045 mg/ml Au) vs solution of an iodine-based clinical regent (350 mg/ml iodine) and saline. Notably, iodine reagents lack absorbance in the near-infrared that could allow remote photothermal heating. B) Photothermal heating comparison between PEG-Nanorods, iodine, and saline monitored using infrared thermography (810 nm NIR light, 2 W/cm^2).

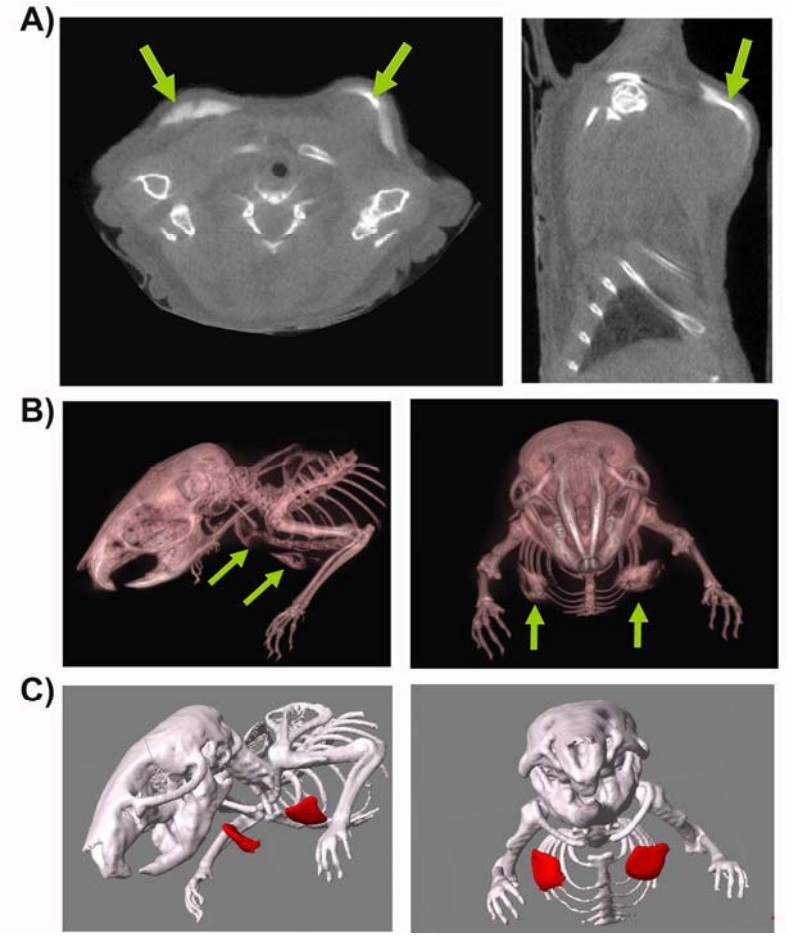

Supplementary Figure 5: *Linking PEG-Nanorod X-ray Tomography with Computational Modeling.* A) Transverse and sagittal slices showing PEG-Nanorod distributions following intratumoral administration into bilateral breast tumors B) 3D reconstructions depicting geometry of PEG-NR injections C) Importation of 3D x-ray CT data into geometries for 4D photothermal modeling (red= PEG-nanorods, white=skeletal structure).

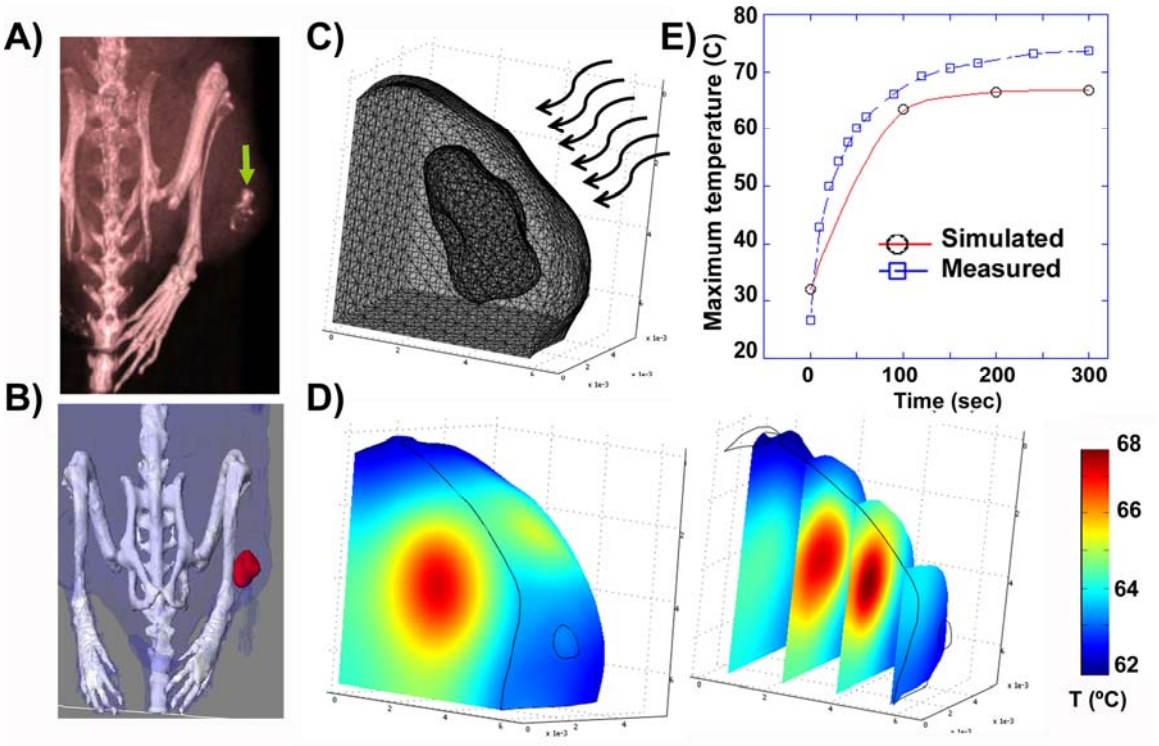

Supplementary Figure 6: *X-ray CT-Fused Computational Modeling of Photothermal Tumor Heating.* A) X-ray CT image of PEG-Nanorod distribution in tumor B) A 3D solid model of the complete geometry was reconstructed by image processing for use with computational photothermal modeling. C) Meshed geometry of the injected tumor chosen as the computational domain with laser orientation and intensity matching that used (1 W/cm^2) (laser direction signified by curved arrows) D) Plot of theoretical surface temperature distribution (left) and the internal predicted temperature profiles inside the computational geometry of the tumor (right) 240 sec following the onset of irradiation. E) Graphical comparison between simulated and thermographically measured maximum surface temperatures over time after the onset of irradiation.

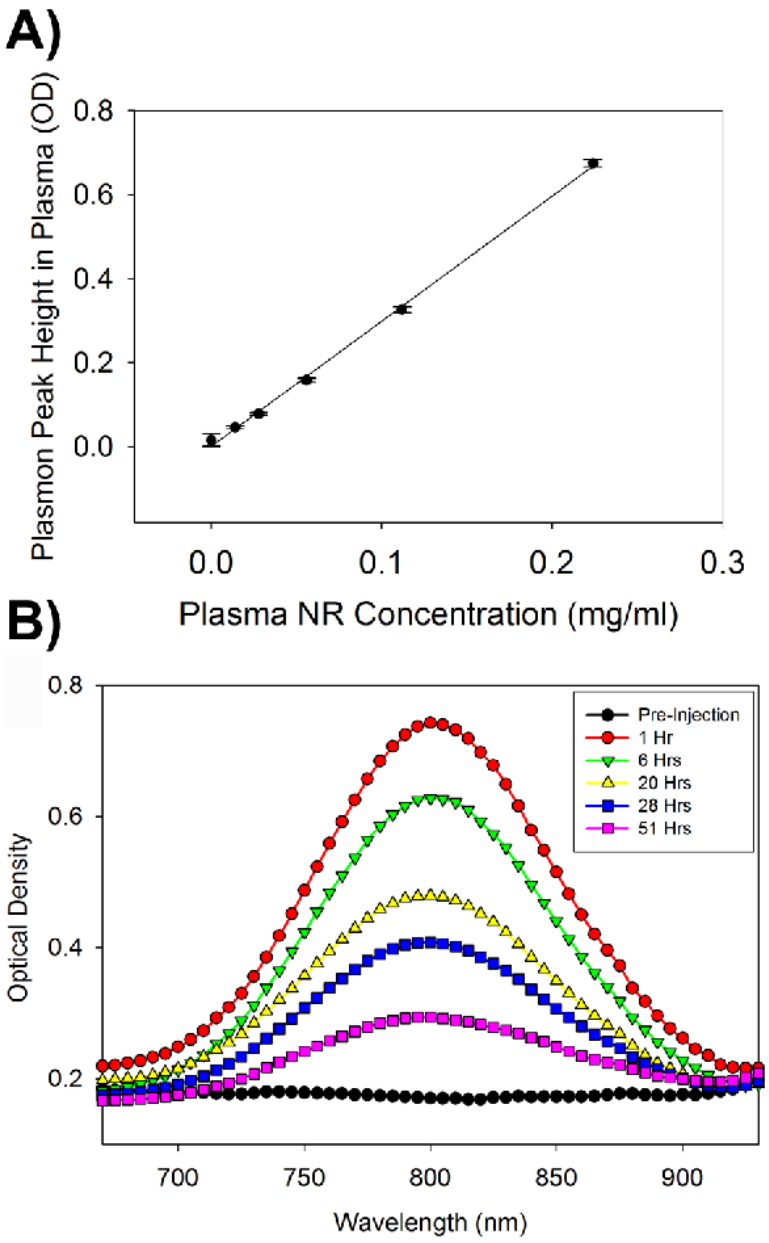

Supplementary Figure 7: *Assessing PEG-NR concentration in plasma via plasmon resonance peak height.* A) PEG-NRs at various concentration were diluted into plasma and spectrophotometrically analyzed to assess NR concentration via the NIR plasmon resonance peak. NRs could be rapidly quantified between ~0.2 mg/ml (the approximate concentration in plasma immediately following injection in mice) and ~0.02 mg/ml. B) Following injection, this method could be applied to rapidly detect PEG-NRs in the plasma of injected mice over time, showing that PEG-NRs maintain their plasmon resonance throughout their blood circulation *in vivo*.

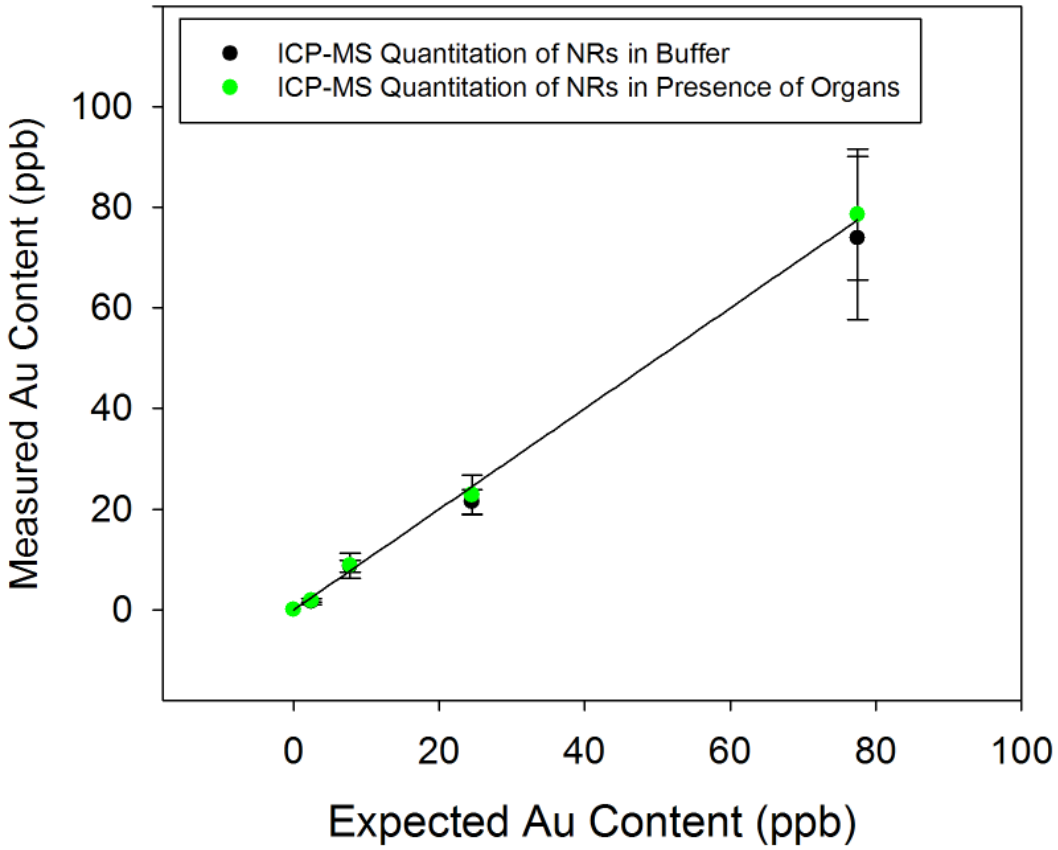

Supplementary Figure 8: *Assessing PEG-NR concentration in organs via ICP-MS Au quantitiation.* PEG-NRs at various concentration were diluted into buffer or into glass vials containing 200 mg sections of liver. Samples were all prepared for ICP-MS quantitation to assess the linearity of Au detection and whether the presence of organs affected quantitation. The samples were made to approximate a range of ~2% to 70% ID/g for 200 mg tissues. Results are plotted for triplicate samples and plotted against the ideal relationship of y=x.

Supplemental Table 1. *Tabular Representation of PEG-NR Biodistribution Data from Figure 5B.*

Tissue	% ID / gram tissue	Standard Deviation
tumor	7.1	+/- 2.9
brain	0.5	+/- 0.3
bladder	0.4	+/- 0.1
muscle	1.7	+/- 0.8
heart	2.4	+/- 0.9
lung	4.4	+/- 0.9
kidney	4.0	+/- 0.3
liver	14.0	+/- 4.0
spleen	51.9	+/- 13.0

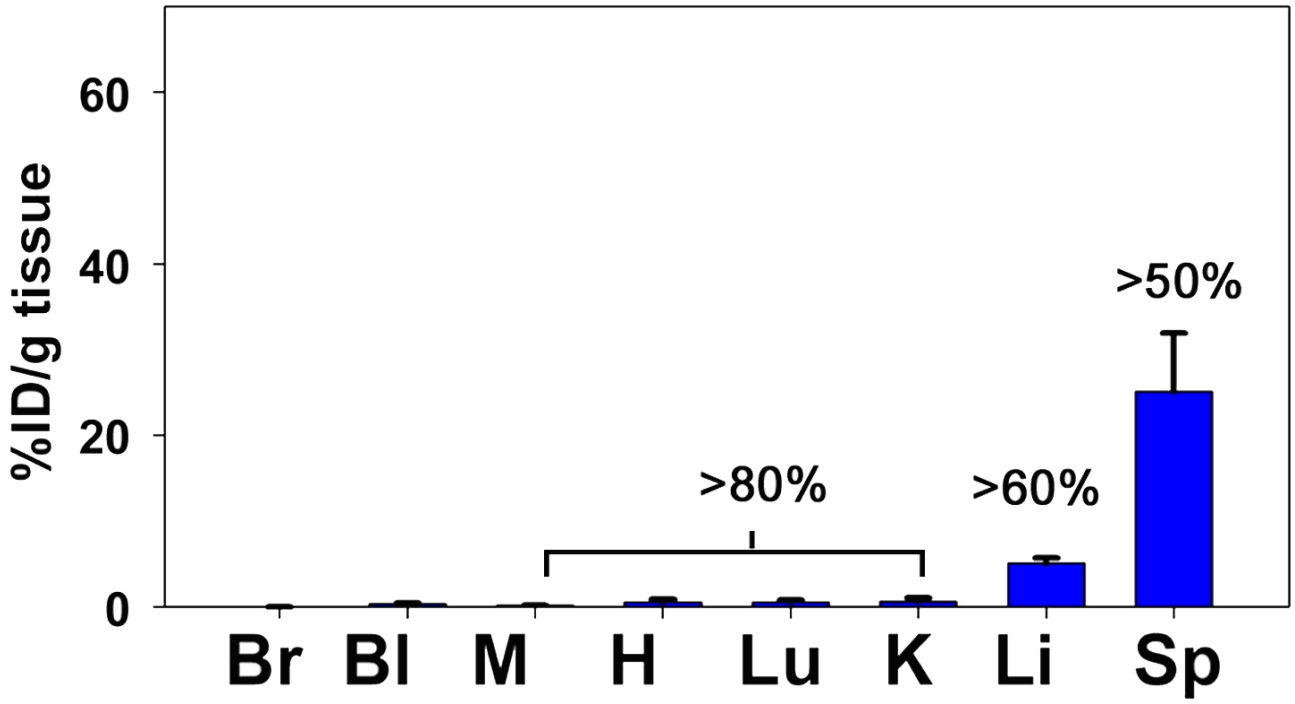

Supplementary Figure 9: *PEG-NR biodistribution in tumor-free mice at 2 months following intravenous injection.* PEG-nanorod biodistribution 2 months following intravenous administration, quantified via ICP-MS (3 mice). Percent values indicate the clearance (or decrease in %ID/g) that occurred during this time period compared to values of organs collected 72 hrs after particle injection (Br=brain, Bl=bladder, M=muscle, H=heart, Lu=lung, K=kidney, Li=liver, Sp=spleen).

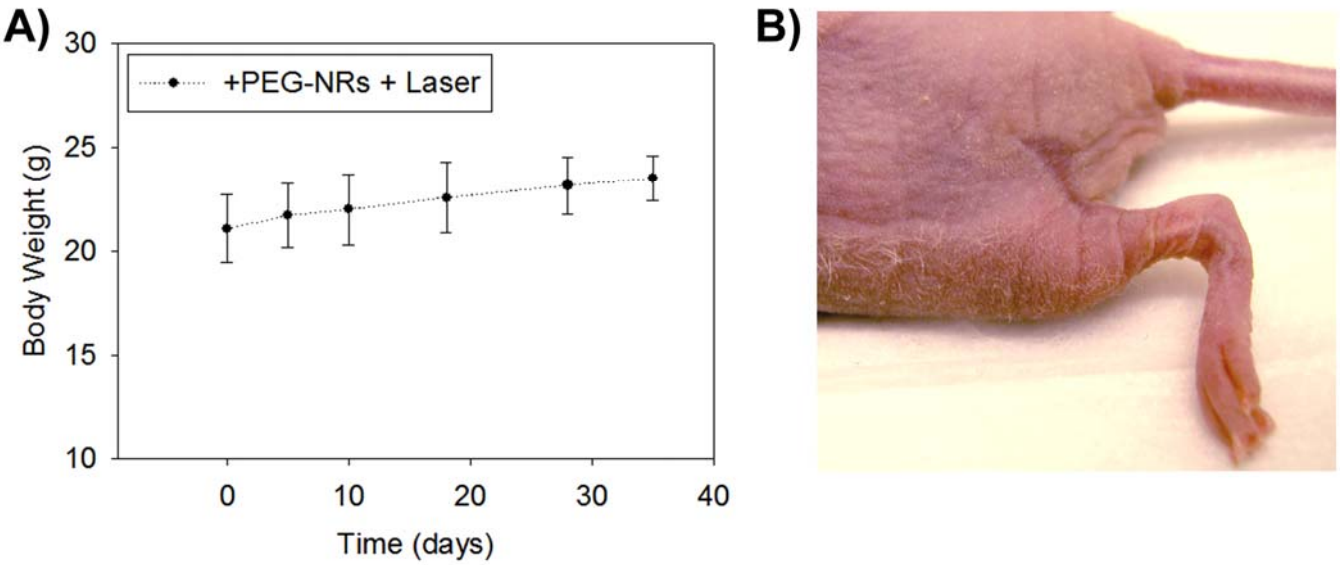

Supplementary Figure 10: *Weight of irradiated, PEG-NR-injected mice during tumor resorption following treatment.* A) Body weight curve of mice bearing unilateral MDA-MB-435 tumors from the survival study (Figure 5C). No obvious body weight loss was observed following PEG-NR-mediated tumor therapy. C) Close view of site of tumor resportion showing only evidence of minor scar.

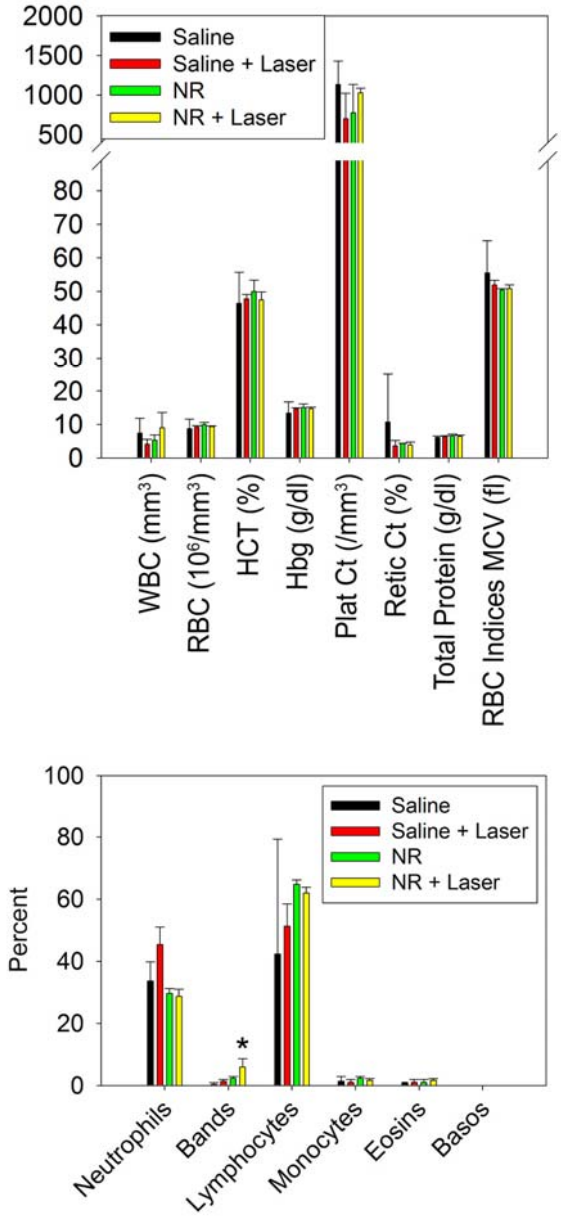

Supplementary Figure 11: *Hematological effects of PEG-NR irradiation in mice.* To explore the effects of NR administration and near-infrared ablation, mice bearing bilateral MDA-MB-435 tumors were injected with either saline or PEG-NRs and, 72 hrs later, either exposed to the therapeutic tumor irradiation protocol under anaesthetic (~2 W/cm^2, 5 min, 810 nm) or anaesthetized without irradiation (n=3 each set). Following irradiation or comparable time under anaesthetic, blood was collected for hematology and mice were sacrificed. The only statistically-significant change observed in response to NR-mediated tumor ablation was a slight increase in the percent of band neutrophils ($p<0.05$ for NR+ Laser vs NR, Saline + Laser, and Saline), likely due to an acute inflammatory response to tumor ablation.

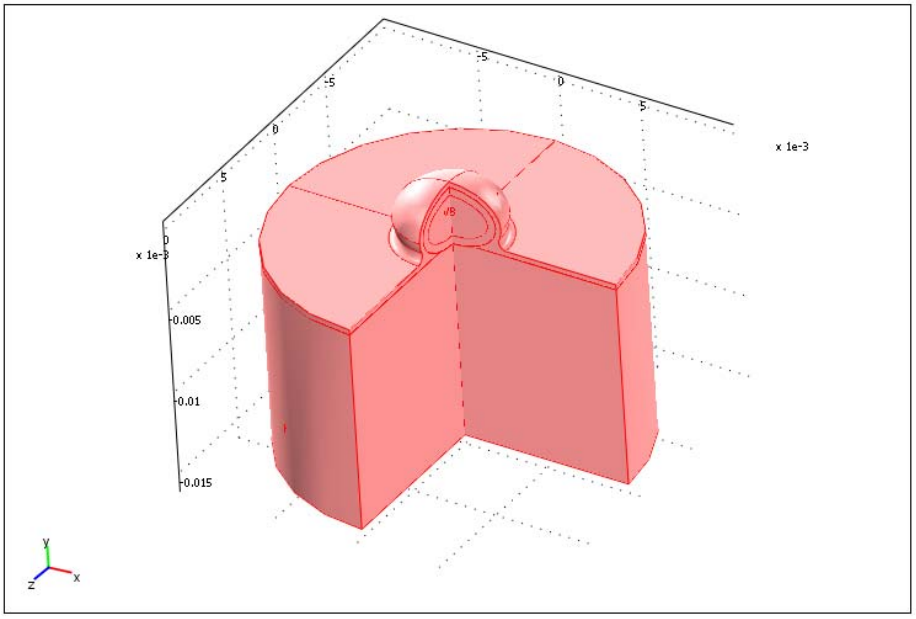

Supplementary Figure 12: *Compuatational domain for modeling photothermal therapy following intravenous administration of PEG-Nanorods.* For intravenous photothermal modeling, a cylindrical domain of 20 mm diameter around the tumor with a depth of 12 mm for the muscle domain was considered for computation. The outer shell of the tumor was considered to be of 0.5 mm thickness.

Finite Element Modeling of Photothermal Tumor Heating

To reveal the magnitude and kinetics of *in vivo* photothermal heat generation by the nanorods and native tissue, the temporal and spatial propagation of thermal gradients, and to assess the timescale within which the entire tumor volume would reach ablative temperatures, a finite element computer simulation of the photothermal ablation process was developed and carried out. The tumor was approximated as a paraboloid, resting above the muscle and covered by skin of 300 μm thickness. The bio-heat transfer equation of Pennes (1948) was applied to the computational domain in the form:

$$\rho c\,(\partial T/\partial t) + \nabla . (-k \nabla T) = \rho_b c_b w_b (T_b - T) + Q_{met} + Q_{laser}$$

Where, ρc is the heat capacity of the muscle, tumor periphery, tumor core or skin as appropriate in the respective regions. The heat capacity of blood is $\rho_b c_b$ and its perfusion rate in the respective domain is w_b. Q_{met} and Q_{laser} are the metabolic and laser heat generation in the tissues respectively. For intravenous photothermal modeling, a cylindrical domain of 20 mm diameter around the tumor with a depth of 12 mm for the muscle domain was considered for computation. The shell of the tumor was considered to be of 0.5 mm thickness having higher rate of blood perfusion than the tumor core. A cut view of the computational domain is shown in Fig S10.

The blood perfusion rate is known to be different in tumor periphery, tumor core, healthy tissues and skin. Hence, they have been taken accordingly from literature (Fujita et al., 1998) as follows

$w_b = F\,[1]$ for $T < 39^0C$

$= F[1+ (p-1)\,(T-39)/(45-39)]$ for $39^0C < T < 45^0C$

$= F[p- (p-1)\,(T-45)/(51-45)]$ for $45^0C < T < 51^0C$

$= F\,[1]$ for $T > 51^0C$

The maximum perfusion rate and the parameter p for different region are given as

Tissue	F (m^3/kg/s)	p
Tumor core	5×10^{-7}	1
Tumor periphery	1.67×10^{-6}	2
Muscle	8.3×10^{-6}	9

Skin	8.3×10^{-6}	9

The thermophysical properties of various regions were taken from accepted values as

Tissue	Density	Specific heat	Thermal conductivity
	m^3/kg	J/(kgK)	W/(mK)
Tumor core	1050	3700	0.5
Tumor periphery	1050	3700	0.5
Muscle	1050	3700	0.5
Skin	1200	3700	0.2
Blood	1000	4200	-

The metabolic heat generation rate is taken to be 400 W/m^3.

Laser heat generation in tissues is a widely studied area. Welch (1984) gave a good overview of the various models available in this area. Seeing various possibilities, the following equation for heat generation, which is a modification of his equation (12) for the present geometry, was chosen:

$$Q_{laser} = \alpha I_0 \exp[-r^2/[2\sigma(0) \exp(\beta z_c)]]\exp[-(\alpha+\beta)z_c]$$

Where I_0 is the laser irradiation intensity in W/m^2, r is the radial distance from the center, and z_c is the depth of the location from the skin. The parameters α and β are the absorption and scattering coefficient (in m^{-1}) of the tissues respectively. To incorporate the curvature of the tumor's surface and the internal multi-layer tissue structure (skin, tumor), the following modification was made:

$$Q_{laser} = \alpha I_0 \exp[-r^2/[2\sigma(0) \exp(\beta z_c)]]\exp[-(\alpha+\beta)(z_c-c-d)] \exp[-(\alpha_s+\beta_s)(z_s)] \exp[-(\alpha_t+\beta_t)z_t]$$

Here, c is the depth of the skin surface from the tumor vertex at a given radial position, d is the depth of the normal tissue above a location, z_s is the depth of the skin above a location and z_t is the depth of the tumor tissue above a location. The suffixes: s and t indicate skin and tumor absorption and scattering

coefficients, respectively; the values of which were taken to be 0.4 and 5.3 cm^{-1} in absence of nanorods (Motamedi et al.(1983)). For the experiments with nanorods, the absorption coefficient of the tumor was predicted to be 3.07 cm^{-1} based on the Nrod biodistribution data (~7% ID/g; 20 mg/kg injected dose; 0.1 cm^3 tumor volume) and *in vitro* absorption measurements. Jain et al (2006) showed that the extinction coefficient of ~13 nm x 47 nm nanorods is dominated by absorption and hence we assumed that nanorods only enhance the tumor absorption coefficient, with insignificant alteration of large endogenous scattering coefficients. The surface heat loss coefficient to the environment was taken as 15 W/m^2K, which is a typical value for natural convection on planar surfaces.

Finite element method (FEM) using the multiphysics enabled software COMSOL was used for modeling. After careful grid variation, a total of 4436 triangular elements per half symmetry plane was chosen to represent tumor heating. The temperature tolerance was at the default value of 0.0001 and a direct matrix inversion technique was used.

Simulation of localized injected nanorod geometry using X-Ray tomography data

For the purpose of simulating the 3D geometry of injected nanorods and the resulting thermal flux upon irradiation, a multi-step procedure was performed to translate 3D X-ray CT images into a form amenable to computational modeling of photothermal heating. For the present cases, 406 DICOM slices were exported, including the tumor, muscle, and the internal skeletal details, as well as the distribution of injected nanorod solutions as shown in Fig. 3 and supplementary Figs. 5 and 6. Subsequently these data were imported in the image processing software Scan IP and reconstructed based on the grey scale values of the scan to form volumetric geometries for nanorods, skeletal structures, and soft tissues as shown in Fig. 3D supplementary Figs.5C and 6B. Next, the solid model was imported to the meshing software Scan FE and proper surface meshing was carried out. Finally, the 3D meshed geometries were imported to COMSOL Multiplysiscs and the thermal analysis was carried in an identical fashion to the previous description in the ellipsoidal geometry.

Results and discussions

Together, the data presented in Figs. 3, 4, S5, and S6 provide considerable evidence that the strategy of utilizing nanoantenna biodistribution data to empower computational irradiation regimen design has the potential to benefit the understanding of nanoantenna function *in vivo*. Particularly, given the large

number of uncertainties in biological systems with respect to parameters such as the precise delineation of underlying muscular tissues, the temperature dependence of thermophysical properties of tissues, variable blood perfusion, and precise tumor geometries (for intravenous cases), it is promising that prediction of the model is kinetically and quantitatively similar to measurements over the given range of parameters. The current work also motivates the future use of 3D methods for temperature measurement *in vivo*, such as the use of MRI. Efforts to integrate controlled NIR-irradiation conditions with MR imaging are beginning and will surely empower future improvements in model optimization.

It is additionally worth discussing the biophysical tissue characteristics that assist in focusing thermal energy within the tumor volume. Particularly, the blood perfusion rates in tumor and normal tissue are enhanced (although with different magnitudes) with increased tissue temperatures up to approximately 45^0C, allowing more efficient heat dissipation for moderate thermal gradients (Fujita et al., 1998). However, beyond 45^0C, tumor blood perfusion drops precipitously, causing tumoral heat dissipation to be diffusion limited. Meanwhile the thermal enhancement of peripheral tissue perfusion by up to 9-fold (see equations for w_b) allows more efficient peripheral cooling. These effects (internal tumor vessel shutdown and enhanced peripheral cooling) work in concert to focus the thermal accumulation within the tumor tissue and amplify the heating specificity imparted by the targeted nanoantennas. These effects will be directly investigated in future work using techniques that enable perfusion measurement during irradiation.

References

Fujita S., M.Tamazawa and K. Kuroda, *IEEE Trans. Biomedical Engg* , 1998, 45, 1182-1186.

Jain P.K., K.S. Lee, I.H.El-Sayed and M.A.El-Sayed, *J.Phys.Chem.B* ,2006,110,7238-7248.

Motamedi M. , T.J White and A.J. Welch , Laser Inst. Amer. ,Los Angeles, CA,1983.

Peennes H.H., *J. Appl. Physiology*, 1948, 1, 93- 122.

Welch A.J., *IEEE J. Quantum Electronics,* 1984, 20,1471-1481.